Spinal cord macrophage glutaminolysis controls glucose homeostasis by supporting sympathetic tone of thermogenic adipose depots.

Johanna Merlin[1*], Stoyan Ivanov[1*], Alexey Sergushichev[2], Marion Ayrault[1], Nathalie Vaillant[1], Jérome Gilleron[3], Mireille Cormont[3], Jean-Francois Tanti[3], Karine Dumas[3], Michael Ohanna[3], Justine Masson[4], Inna Gaisler-Salomon[4], Stephen Rayport[4], Diane B Re[5], Emmanuel L. Gautier[6], Rodolphe Guinamard[1], Maxim N Artyomov[7], Laurent Yvan-Charvet[1]

*These authors contributed equally to this work

[1]Institut National de la Santé et de la Recherche Médicale (Inserm) U1065, Université Côte d'Azur, Centre Méditerranéen de Médecine Moléculaire (C3M), Atip-Avenir, Fédération Hospitalo-Universitaire (FHU) Oncoage, 06204 Nice, France (J.M., S.I., M.A., N.V, R.G., L.Y.C.)

[2]Computer Technologies Department, ITMO University, Saint Petersburg, Russia (A.S.)

[3]Université Côte d'Azur, Institut National de la Santé et de la Recherche Médicale (Inserm) U1065, Centre Méditerranéen de Médecine Moléculaire (C3M), Team 1 and 7, 06204 Nice, France (J.G., M.C., J.F.T., K.D., M.O.)

[4]Department of Psychiatry, Columbia University, USA; Department of Molecular Therapeutics, NYS Psychiatric Institute, USA (J.M., I.G.S., S.R.)

[5]EHS Department and Motor Neuron Center, Columbia University, 630W 168th Street Suite 16421-B, New York, NY, 10032, USA (D.B.R)

[6]Sorbonne Université, INSERM, UMR_S 1166 ICAN, F-75013 Paris, France (E.G.)

[7]Department of Pathology and Immunology, Washington University School of Medicine, St. Louis, MO, USA (M.N.A.)

Address correspondence to LYC: yvancharvet@unice.fr

Short title: Macrophage glutaminolysis and thermogenesis

Keywords: Macrophage, Glutaminolysis, Thermogenesis, Glucose tolerance, Adipose tissue, Glutamatergic and Sympathetic tones.

Abstract

Adipose tissue dysfunction causes metabolic diseases, including glucose intolerance. Adipose tissue macrophages (ATMs) are important sentinels that control the expandability of visceral adipose tissue and thermogenesis in inguinal and brown adipose depots. The underlying mechanisms that regulate these alterations, however, are still poorly defined. Here, we report that mice with defective macrophage glutaminolysis displayed glucose intolerance independent of excessive visceral fat inflammation and storage. Reduced glucose influx was associated with impaired norepinephrine-dependent thermogenic responses of subcutaneous and brown adipose tissue. This phenomenon was associated with upstream perturbation of neuronal activation in the spinal cords of mice deficient in macrophage glutaminolysis, which is required for activation of sympathetic tone-dependent thermogenesis. Mechanistically, we found that altered glutaminolysis reprogrammed spinal cord macrophage metabolism and limited the fusiform projections of macrophages, which are hallmarks of neuronal contacts, *in vitro* and *in vivo*. Collectively, our study reveals a previously unappreciated homeostatic role for spinal cord macrophage glutaminolysis in the control of sympathetic tone in thermogenic adipose depots. Disruption of these circuits results in metabolic imbalance.

Introduction

Macrophages, which maintain tissue homeostasis and integrity, are present in all organs (Okabe and Medzhitov, 2016). In healthy adipose tissue, macrophages are the numerically dominant immune cell type (Lumeng et al., 2007; Weisberg et al., 2003; Xu et al., 2003). The diverse functions of visceral adipose tissue macrophage (vATM) subsets, ranging from regulation of lipid metabolism to sampling of blood material in visceral white adipose tissue (vWAT), have been documented (Jaitin et al., 2019; Lumeng et al., 2008; Silva et al., 2019; Xu et al., 2013). Macrophages have also been observed in subcutaneous white adipose tissue (ScWAT) and in brown adipose tissue (BAT), where they are involved in nonshivering thermogenesis. Indeed, these macrophages regulate sympathetic tone associated with the high innervation density of these thermogenic adipose depots (Ivanov et al., 2018; Kajimura et al., 2015; Reitman, 2017). Mechanistically, these macrophages can limit sympathetic tone-mediated thermogenesis by expressing PlexinA4, which repulses Sema6A-expressing sympathetic axons, thus controlling BAT neuron density (Wolf et al., 2017). A recent report also suggested that sympathetic neuron-associated macrophages can locally reduce norepinephrine (NE) availability through its uptake and subsequent degradation, which represents an alternative mechanism of thermogenesis regulation (Pirzgalska et al., 2017). However, the metabolic regulation of these processes remains poorly understood.

At the molecular level, macrophage effector functions and metabolic processes are intertwined and constitute integral components of metabolic complications (Artyomov et al., 2016; Mills et al., 2017; Puleston et al., 2017; Stienstra et al., 2017). Perturbation of glutamine metabolism links obesity to inflammation in vWAT (Petrus et al., 2020), and although its use is controversial, glutamine supplementation can improve weight loss and metabolic health (Opara et al., 1996; Laviano et al., 2014; Ramezani Ahmadi et al., 2019). Network integration of parallel *in vitro* high-throughput metabolomic and transcriptomic data has revealed that glutaminolysis is central to alternative macrophage polarization (Jha et al., 2015). This finding could explain why glutamine administration attenuates proinflammatory profiles in the visceral fat of obese patients (Petrus et al., 2020). The role of glutamine in other adipose depots is unknown, but the thermogenic functions of ScWAT and BAT macrophages are unlikely to be linked to their inflammatory status (Fischer et al., 2017; Nguyen et al., 2011; Qiu et al., 2014). Thus, the causal relevance of macrophage glutaminolysis *in vivo*, both at steady state and during metabolic inflammation, remains poorly understood.

Macrophage glutaminolysis relies on the enzyme glutaminase (Gls) 1, which hydrolyzes glutamine into glutamate. To test the causal relationship between modulation of glutamine catabolism, ATM behavior and metabolic homeostasis, we generated and characterized myeloid cell-specific *Gls1*-deficient ($Lyz2^{cre}$ x $Gls1^{flox}$) mice. The elimination of macrophage glutaminolysis in mice resulted in a proinflammatory phenotype in vWAT, which was associated with higher visceral adiposity, but not in other adipose depots upon exposure to a high-fat diet (HFD). However, this phenotype is likely not the culprit of the systemic metabolic perturbations in these mice since glucose intolerance was also observed in $Lyz2^{cre}$ x $Gls1^{flox}$ mice fed a regular chow diet and was associated with impaired homeostatic energy expenditure due to perturbed BAT and ScAT thermogenesis. Malfunction of thermogenic adipose depots was the consequence of reduced sympathetic tone in mice with defective macrophage glutaminolysis and was associated with upstream perturbation of neuronal circuits in the spinal cord. Indeed, the metabolic reprogramming of *Gls1*-deficient spinal cord macrophages promoted a decrease in cell projections and the expression of molecules associated with the microtubule cytoskeleton reorganization machinery. These changes dampened the release of the excitatory neurotransmitter glutamate, which is required for activation of sympathetic tone. Collectively, our findings suggest that macrophage glutaminolysis governs glucose homeostasis through the previously unknown homeostatic role of spinal cord macrophages in the control of glutamatergic neuron activation and subsequent sympathetic tone of thermogenic adipose depots.

Results

Macrophage Gls1 deficiency promotes metabolic imbalance and glucose intolerance. To investigate the potential contribution of macrophage glutaminolysis to energy homeostasis, mice with macrophage-specific Gls1 deficiency ($Mac^{\Delta Gls1}$ mice) and their controls were fed standard chow or a HFD for 12 weeks. $Mac^{\Delta Gls1}$ mice developed normally and exhibited similar body weight gain as control mice, even when the mice were fed a HFD (**Fig. S1A**). Nevertheless, standard chow- and HFD-fed $Mac^{\Delta Gls1}$ mice exhibited a lower respiratory quotient (RQ) profile during the nocturnal period than standard chow- and HFD-fed control mice, as measured by indirect calorimetry (**Fig. 1A**). This finding could explain the lower energy expenditure observed in $Mac^{\Delta Gls1}$ mice fed either standard chow or a HFD (**Fig. 1B**), as food intake was not consistently different between $Mac^{\Delta Gls1}$ mice and control mice under either diet and locomotor activity was similar between genotypes (**Table. S1**). Notably, pair feeding confirmed that the reduced energy expenditure of standard chow-fed $Mac^{\Delta Gls1}$ mice was independent of food intake (**Fig. S1B**). Consistently, the mRNA expression of genes encoding hypothalamic central regulators of food intake, such as *Pomc*, *Agrp*, *Npy* and *Pth2r,* in the hypothalamus was similar between standard chow-fed $Mac^{\Delta Gls1}$ mice and littermate controls (**Fig. S1C**). Consistent with the observation that the $Mac^{\Delta Gls1}$ mice did not have lower RQ profiles during the postabsorptive period (transition to daily phase), when lipid oxidation occurs (**Fig. 1A**), we excluded the possibility that fatty acid metabolism was altered in these mice. First, we observed that increasing fatty acid oxidation by fasting resulted in similar energy expenditure (**Fig. S1B**). Second, plasma free fatty acid levels were similar between standard chow-fed $Mac^{\Delta Gls1}$ mice and their littermates after a fasting/refeeding protocol (**Fig. S1D**). Additionally, a similar percentage of gastrocnemius skeletal muscle oxidative fibers was observed in HFD-fed $Mac^{\Delta Gls1}$ mice and HFD-fed control mice (**Fig. S1E**). Finally, liver morphology (**Fig. S1F**), the levels of plasma alanine transaminase (ALAT) and aspartate transaminase (ASAT), which are hepatotoxicity markers (**Fig. S1G**), and triglyceride content (**Fig. S1H**) were unaltered in $Mac^{\Delta Gls1}$ mice compared to control mice. In contrast, $Mac^{\Delta Gls1}$ mice exhibited a ~20% decrease in glucose oxidation compared to that in control mice when fed standard chow or a HFD (**Table. S1**). We next found that administration of an intraperitoneal bolus of glucose resulted in delayed substrate clearance from the peripheral blood circulation in mice lacking Gls1 in macrophages. This was observed in both standard chow -fed (**Fig. 1C**) and HFD-fed $Mac^{\Delta Gls1}$ mice (**Fig. 1D**). Quantification of the area under the curve confirmed that glucose utilization was perturbed (**Figs 1C and 1D**). Analysis of homeostatic model assessment- insulin resistance (HOMA-IR) indexes suggested that this perturbation occurred with little effect on insulin sensitivity (**Fig. 1E**). Similar insulin levels were observed at baseline and 20 minutes after glucose injection in HFD-fed $Mac^{\Delta Gls1}$ mice (**Fig. S1I**). Thus, impaired glucose tolerance in mice with macrophage glutaminolysis deficiency was most likely the consequence of reduced peripheral glucose clearance.

Brown adipose tissue rather than visceral fat couples macrophage-specific Gls1 deficiency to glycemic control. Increased vATM infiltration and a switch from the alternatively activated phenotype to the proinflammatory phenotype are hallmarks of metainflammation and metabolic perturbations (McNelis and Olefsky, 2014; Odegaard and Chawla, 2015; Rosen and Spiegelman, 2014), and a role for glutamine in vWAT inflammation has recently emerged (Petrus et al., 2020). We first observed that macrophage Gls1 deficiency perturbed glutaminolysis in the vWAT of standard chow-fed mice but not in other adipose depots, as shown by higher glutamine (Gln) and lower glutamate (Glu) levels in vWAT than in other adipose tissues (**Fig. S1K**). Taking advantage of publicly available gene expression datasets (Choi et al., 2015; Fitzgibbons et al., 2011), we also observed that HFD feeding lowered *Gls1* mRNA expression specifically in vWAT and that this decrease paralleled a decrease in the expression of alternatively activated macrophage markers and an increase in the expression of proinflammatory markers (**Fig. S1J**). Thus, we next characterized the

phenotype of vWAT in Mac$^{\Delta Gls1}$ mice to determine whether it is associated with impaired glucose tolerance in these mice. Surprisingly, we did not observe significant changes in fat mass (**Fig. S1L**) or ATM number (**Fig. S1M**) in any adipose depots, including vWAT, of standard chow-fed Mac$^{\Delta Gls1}$ mice. In contrast, we observed specific increases in vWAT mass (**Fig. S1L**) and vATM number (**Fig. S1M**) when Mac$^{\Delta Gls1}$ mice were challenged with a HFD. Morphological examination showed that the vWAT of HFD-fed Mac$^{\Delta Gls1}$ mice contained larger adipocytes and confirmed that macrophage infiltration was enhanced, as illustrated by the appearance of characteristic crown-like structures (**Fig. S1N**). Additionally, an imbalance in the expression of alternatively activated (*Mrc1* and *Retnla*) and proinflammatory (*Cd68*, *Tnf*α, and *Hmox1*) macrophage markers was observed in the vWAT of HFD-fed Mac$^{\Delta Gls1}$ mice (**Fig. S1O**) but not in ScWAT or BAT (**Fig. S1P**). This change was associated with reduced AKT phosphorylation, suggesting that inflammatory cell infiltration participated in local insulin resistance in the vWAT of HFD-fed Mac$^{\Delta Gls1}$ mice (**Fig. S1Q**). To delineate whether this effect can explain the glucose intolerance of Mac$^{\Delta Gls1}$ mice, we next examined the uptake of the radiolabeled D-glucose analog 2-[^{14}C]-deoxyglucose (2-[^{14}C]-DG) in these mice. No significant changes were observed in the total uptake of 2-[^{14}C]-DG in the brain, skeletal muscle, pancreas or ScWAT of standard chow- and HFD-fed control and Mac$^{\Delta Gls1}$ mice (**Fig. 1F, left panel**). Total 2-[^{14}C]-DG incorporation in vWAT was higher in HFD-fed Mac$^{\Delta Gls1}$ than in standard chow-fed Mac$^{\Delta Gls1}$ mice, correlating with vWAT mass, but as expected, the rate constant for net tissue uptake of 2-[^{14}C]-DG was reduced (**Fig. 1F, right panel**). This latter finding was consistent with local insulin resistance observed in the vWAT of HFD-fed Mac$^{\Delta Gls1}$ mice and partially contributed to the glucose intolerance of these mice under HFD conditions. However, this finding could not explain the glucose intolerance observed in standard chow-fed mice. Unexpectedly, both the total uptake and rate constant of 2-[^{14}C]-DG were indeed decreased by two- to three-fold in the intrascapular BAT of standard chow- and HFD-fed Mac$^{\Delta Gls1}$ mice compared to standard chow- and HFD-fed control mice (**Figs. 1F**). Altogether, our observations identify a previously undescribed role of macrophage glutaminolysis in controlling BAT glucose utilization, which most likely participates in improving glucose tolerance through energy dissipation.

Defective macrophage glutaminolysis leads to impaired homeostatic nonshivering thermogenesis. Glucose fuels sympathetic nervous system-induced nonshivering thermogenesis (Orava et al., 2011; Stanford et al., 2013). Thus, we first quantified NE levels in different adipose depots. A decrease in NE levels was observed in both the ScWAT and BAT of standard chow- and HFD-fed Mac$^{\Delta Gls1}$ mice compared to controls (**Fig. 2A**). This change was not observed in vWAT (**Fig. 2A**). To test the *in vivo* relevance of these findings, we next measured heat production in Mac$^{\Delta Gls1}$ mice. Indirect calorimetry measurements (Wolf et al., 2017) showed that standard chow-fed Mac$^{\Delta Gls1}$ mice displayed significantly lower energy dissipation through heat production than their littermate controls (**Fig. 2B**). A trend towards lower heat production was also observed in HFD-fed Mac$^{\Delta Gls1}$ mice during the nocturnal period (**Fig. 2B**). Nonshivering thermogenesis is dependent on the high expression levels of uncoupling protein 1 (*Ucp1*), PR-domain containing 16 (*Prdm16*), type II deiodinase (*Dio2*), peroxisome proliferator–activated receptor coactivator Pgc1α (*Ppargc1*α), cell death activator-A (*Cidea*) and β3 adrenergic receptor (*Adrb3*), which are highly expressed in ScWAT and BAT, to support energy metabolism and shunt energy generated by mitochondria from ATP to thermogenesis (Chechi et al., 2013). Lower expression of *Ucp1*, *Ppargc1*α and *Cidea* was observed in the ScWAT of HFD-fed Mac$^{\Delta Gls1}$ mice than in the HFD-fed control mice (**Fig. S2A**). Further histological analysis of ScWAT revealed fewer clusters of multilocular brown fat-like areas and more unilocular regions in HFD-fed Mac$^{\Delta Gls1}$ mice than in HFD-fed control mice (**Fig. S2B**). Thus, macrophage glutaminolysis participated to some extent in ScWAT browning. More strikingly, downregulation of most of the genes involved in thermogenesis was observed in the BAT of both standard chow- and HFD-fed Mac$^{\Delta Gls1}$ mice compared to that of littermate controls (**Fig. 2C**). Consistently, larger lipid droplets in brown adipocytes were observed in chow- and HFD-fed Mac$^{\Delta Gls1}$ mice than in control animals (**Fig. 2D**). The BAT temperature of Mac$^{\Delta Gls1}$

mice also decreased by approximately 1°C at steady state (**Fig. S2C**). These results suggest that macrophage glutaminolysis dominantly controls nonshivering thermogenesis through local availability of NE in BAT.

Macrophage glutaminolysis controls sympathetic tone independent of macrophage-adipocyte interactions, sympathetic innervation and catecholamine catabolism. Several macrophage-dependent mechanisms are involved in thermogenic function. First, vascular cell adhesion molecule-1 (VCAM-1) on macrophages can directly interact with its ligand integrin α4 (ITGA4) on adipocytes to limit beige adipogenesis (Chung et al., 2017). Consistent with the lack of differential inflammation, we failed to observe changes in the mRNA expression of *Vcam1* and *Itga4* between the ScWAT and BAT of Mac$^{\Delta Gls1}$ mice and those of control mice (**Fig. S3A**). BAT macrophages can also modulate the attraction of sympathetic axons (Wolf et al., 2017), which are known to innervate adipose depots and control NE-dependent thermogenesis (Cannon and Nedergaard, 2004; Nguyen et al., 2014; Nguyen et al., 2018). To address the role of sympathetic tone, we chemically denervated the sympathetic nervous system by injection of 6-hydroxydopamine (6-OHDA), a hydroxylated analog of dopamine (Cao et al., 2019; Nguyen et al., 2017). Treatment with 6-OHDA lowered BAT NE levels to the same extent in control and Mac$^{\Delta Gls1}$ mice (**Fig. 3A**). Consequently, by reducing energy expenditure (**Fig. S3B**) and heat production (**Fig. 3B**), 6-OHDA treatment abolished the differences between control and Mac$^{\Delta Gls1}$ mice. Transcriptomic analysis of genes involved in nonshivering thermogenesis in BAT confirmed that following chemical denervation, the expression of Ucp1, Pgc1α and Prdm16 was similar in both genotypes (**Fig. S3C**). These findings suggest that reduced sympathetic tone in Mac$^{\Delta Gls1}$ mice could be the cause of defective NE-dependent thermogenesis in these mice. However, the trend towards reduced tyrosine hydroxylase (Th) staining in the BAT of CD-fed Mac$^{\Delta Gls1}$ mice compared to that of control mice was nonsignificant, and analysis of axons in the sympathetic autonomic nervous system (Wolf et al., 2017) revealed no difference in sympathetic axon density between HFD-fed Mac$^{\Delta Gls1}$ and HFD-fed control mice (**Fig. 3C**). Consistently, the expression of genes previously shown to control the repulsion of neurons by macrophages, such as the transmembrane semaphorin Sema6a, its ligand Plexin A4 and the transcription regulator methyl-CpG-binding protein 2 (Mecp2) (Wolf et al., 2017), was unaltered in the BAT of Mac$^{\Delta Gls1}$ mice compared to that of control mice (**Fig. 3D**). Similar findings were observed in the ScWAT of Mac$^{\Delta Gls1}$ mice (**Fig. S3D**). The expression of Th was low and not significantly altered in the adipose depots of these mice (**Fig. 3D and Fig. S3D**). Recently, a population of sympathetic neuron-associated macrophages (SAMs) in different adipose depots and in subcutaneous fascia was found to mediate catecholamine catabolism (Camell et al., 2017; Pirzgalska et al., 2017). Low Gls1 mRNA expression was first observed in these SAM populations (**Fig. S3E**). Transcriptomic analysis did not reveal significant changes in genes that regulate catecholamine catabolism between the BAT and ScWAT of standard chow- and HFD-fed Mac$^{\Delta Gls1}$ mice and those of standard chow- and HFD-fed control mice, including the NE transporter Slc6a2 and the monoamine oxidase A (MAOA), which were previously shown to control NE uptake and degradation, respectively (**Fig. 3D and Fig. S3D**). To directly assess the contribution of glutaminolysis to the ability of SAMs to degrade NE, we first visualized SAMs in the subcutaneous fascia based on the expression of CX3CR1 and isolated them by flow cytometry based on the expression of the canonical macrophage markers CD64 and MerTK (**Fig. S3F**). We cultured these cells with exogenous NE in the presence or absence of clorgyline, a selective MAOA inhibitor, as previously described (Camell et al., 2017; Pirzgalska et al., 2017). As expected, MAOA inhibition prevented NE degradation in the culture medium, but Gls1 deficiency had no effect on this process (**Fig. 3E**). Thus, macrophage glutaminolysis controls NE-dependent thermogenesis through a mechanism independent of local inflammation, sympathetic innervation and macrophage catecholamine degradation.

Macrophage glutaminolysis controls spinal cord neuron activation. We next reasoned that sympathetic preganglionic neurons that project to thermogenic adipose depots can be controlled by presynaptic glutamatergic neurons (Morrison and Madden, 2014; Tupone et al.,

2014). These neurons are localized in the intermediolateral nucleus (IML) located between the T2 and T6 segments of the spinal cord (**Fig. 4A**). Quantification of activated neurons by immunoblotting with a c-Fos antibody revealed less neuron activation in the spinal cord of $Mac^{\Delta Gls1}$ mice than in that of control mice (**Fig. 4B**). The level of glutamate, which is a physiological excitatory neurotransmitter, was also decreased in the T2-6 segments of the spinal cord of $Mac^{\Delta Gls1}$ mice compared to controls (**Fig. 4C**). Remarkably, daily *i.p.* administration of glutamate (50 mg/kg) to standard chow-fed $Mac^{\Delta Gls1}$ and littermate control mice for 12 days did not alter body weight (data not shown) but increased postprandial energy expenditure (**Fig. S4A**) and heat production (**Fig. 4D**) in both genotypes and thus rescued the defects observed in $Mac^{\Delta Gls1}$ mice. These observations were mirrored by normalization of NE levels in the BAT of these mice (**Fig. 4E**). We next evaluated whether defective macrophage glutaminolysis plays a role in the spinal cord by investigating the gene expression profile of spinal cord macrophages compared to those of microglia and peritoneal cavity macrophages (PCMs). We sorted these macrophage populations based on the expressed canonical CD64 and CD11b markers (**Fig. S4B**). We confirmed that, similar to microglia (Ajami et al., 2007; Ginhoux et al., 2010; Schulz et al., 2012; Guimaraes et al., 2019), spinal cord macrophages were tissue-resident and not monocyte-derived, as shown by their resistance to radiation and their lack of repopulation after $CX3CR1^{gfp/+}$ (CD45.1) bone marrow transplantation in lethally irradiated CD45.2 control recipients (**Fig. S4C**). Of note, by performing k-means clustering of our gene expression profile data obtained by RNA-seq, we also identified modules containing markers that were expressed by both spinal cord macrophages and microglia (i.e., Cx3cr1) or PCMs (i.e., Cxcl2) and found genes that were not expressed in microglia and PCMs (i.e., Cxcl10, Chil3, Klf4 and Trem3) (**Fig. S4D**). PCA analysis revealed that spinal cord macrophages were transcriptionally distinct from both PCMs and microglia and were strongly impacted by defective glutaminolysis (**Fig. 4F**). Global metabolic transcriptome signatures and topological analyses using CoMBI-T (Jha et al., 2015) also confirmed that defective glutaminolysis metabolically reprogrammed spinal cord macrophages (**Fig. S4E**). To explore the broader effect of Gls1 deficiency on the expression profile of spinal cord macrophages, we constructed a volcano plot. Specifically, 354 genes were upregulated and 124 were downregulated ($-Log_{10}(Pval) > 2$) (**Fig. 4G**). Gene set enrichment analysis (GSEA) of the differentially expressed genes identified 'Microtubule cytoskeleton' and 'Mitochondrion' GO terms as the most enriched terms for genes that were upregulated in glutaminolysis-deficient spinal cord macrophages, while 'Cell projection' and 'Response to stimuli' were enriched for downregulated genes (**Fig. S4F**). To test the *in vivo* relevance of these findings, $Cx3cr1^{GFP/+}$ reporter mice were backcrossed to control and $Mac^{\Delta Gls1}$ mice, and spinal cord tissues were stained for VGLUT3 and DAPI and visualized by confocal microscopy. While control $Cx3cr1^{GFP/+}$ mice exhibited a dense network of fusiform $Cx3cr1^{GFP/+}$ macrophages in the IML region of the spinal cord, $Cx3cr1^{GFP/+}Mac^{\Delta Gls1}$ mice exhibited more rounded $Cx3cr1^{GFP}$ spinal cord macrophages (**Fig. 4H and S4G**). Finally, we cocultured primary $actin^{+}$ neocortical neurons enriched in glutamate with sorted control or Gls1-deficient spinal cord or peritoneal macrophages. As in the *in vivo* experiment, we observed that defective glutaminolysis significantly changed the shape of macrophages; specifically, it decreased the ratio of fusiform to rounded macrophages, suggesting that the macrophages participated in less cellular sensing through their profuse pseudopodia (**Fig. 4I**). Reduced glutamate levels in the coculture medium of Gls1-deficient macrophages was consistent with the lower levels of excitatory neurotransmitters *in vivo* **(Fig. 4J**). Collectively, these data suggest that glutaminolysis deficiency metabolically reprograms spinal cord macrophages, impeding their projections and compromising the glutamatergic tone that governs peripheral thermogenic adipose tissue sympathetic activation.

Discussion

Glutamine links obesity to adipose tissue inflammation (Petrus et al., 2020), but the pathophysiological and causal relevance of this pathway *in vivo* at steady state and during metabolic inflammation remains poorly understood. Using a newly generated genetic mouse model, we first demonstrated a causal role of Gls1-dependent macrophage glutaminolysis in limiting visceral fat inflammation and storage during obesity. Our study also uncovered a novel mechanism by which macrophage glutaminolysis supports glucose tolerance at steady state. Indeed, macrophage glutaminolysis increased glucose oxidation through heat generation and improved homeostatic thermogenesis of subcutaneous and brown adipose depots. This process is increasingly being recognized as a hallmark of metabolic health (Glass and Olefsky, 2012; McNelis and Olefsky, 2014; Murray et al., 2014; Odegaard and Chawla, 2015; Rosen and Spiegelman, 2014; Wynn et al., 2013). Our findings offer a new paradigm explaining how glutaminolysis fine-tunes energy metabolism by playing a previously unrecognized role in spinal cord macrophages, controlling their shape and expression of branching projection genes and supporting glutamatergic transmission, which is required for efficient sympathetic tone-dependent thermogenesis.

When we initiated the present study, we hypothesized that mice with defective macrophage glutaminolysis (i.e., Gls1 deficiency) would induce a switch from an anti-inflammatory to a proinflammatory phenotype in vWAT, leading to *in vivo* fat inflammation and storage, hallmarks of metabolic disease. This hypothesis was driven by observations showing that vATM glutaminolysis is modulated by obesity and inversely associated with the profile of secreted cytokines (Boutens et al., 2018) and that altering macrophage glutamine utilization *in vitro* prevents the promotion of efficient alternative macrophage activation (Jha et al., 2015; Liu et al., 2017). Unlike other adipose depots, WAT was strongly impacted by defective macrophage glutaminolysis, as shown by the increased Gln/Glu ratio in this tissue as well enhanced fat inflammation and storage upon HFD feeding. This finding revealed a causal role of this metabolic pathway in obesity-induced inflammation. The specificity of these regulatory mechanisms for vWAT over other adipose depots requires further investigation. High levels of Gln and Glu in vWAT could provide adequate environmental conditions for these regulatory mechanisms, as was recently shown in the peritoneal cavity (Davies et al., 2017). Consistent with this hypothesis, the mRNA expression of Gls1 in vWAT was high, inversely correlated with the expression of classically activated inflammatory macrophage markers and positively correlated with the expression of alternatively activated macrophage markers. This finding suggests that vATMs may have a specific genetic predisposition to face their local environment. As vATMs are the major immune cells in vWAT, they may specifically interact with visceral adipocytes. For instance, in the vWAT of lean animals, adipocytes constantly release fatty acids into the local microenvironment as sources for macrophage fatty acid oxidation, which is required to support alternative macrophage polarization (Huang et al., 2014). Thus, glutaminolysis may facilitate the generation of anaplerotic reactions to support vATM respiratory burst, as observed in other *in vitro* and *in vivo* settings (Jha et al., 2015; Liu et al., 2017). Downregulation of this pathway upon HFD feeding could reflect perturbed fatty acid oxidation due to a specific program of lysosomal-dependent lipid degradation at the origin of the inflammatory response (Kratz et al., 2014; Xu et al., 2013) or increased recruitment of metabolically immature monocytes from the blood vasculature (Weisberg et al., 2006; (Silva et al., 2019). Although further studies are required to pinpoint the origin of these perturbations, our findings clearly establish that macrophage glutaminolysis causally participates in the crosstalk between vATMs and visceral adipocytes to maintain tissue homeostasis.

Unexpectedly, our results also demonstrate that abrogation of macrophage glutaminolysis in mice results in a broad range of metabolically deleterious effects, particularly impaired glucose tolerance due to lower glucose utilization by thermogenic adipose depots required for nonshivering thermogenesis. Although a switch between alternative and classical macrophage activation is often associated with impaired thermogenesis under conditions of disrupted metabolic homeostasis such as HFD-induced obesity (Ivanov et al., 2018; Reitman,

2017), the present study reveals that reduced thermogenesis occurs under steady state conditions in Mac$^{\Delta Gls1}$ mice independent of any perturbation in ATM activation in thermogenic adipose depots. These findings add to the current debate on the causal contribution of macrophage activation pathways to the regulation of thermogenesis. For instance, alternatively activated macrophages were first reported as a source of catecholamines that act in a paracrine fashion to activate β-adrenergic receptor signaling-dependent thermogenesis in ScWAT and BAT (Nguyen et al., 2011; Qiu et al., 2014). However, this view was recently challenged by Buettner's group, who showed that Th, the rate-limiting enzyme for the synthesis of catecholamines, is not expressed in ATMs (Fischer et al., 2017; Wolf et al., 2017). Additionally, the authors reported that conditioned media obtained from IL-4-stimulated macrophages and chronic *in vivo* IL-4 treatment fail to increase the thermogenic response in adipose tissue (Fischer et al., 2017). Thus, we hypothesized that macrophage glutaminolysis can promote glucose-dependent nonshivering thermogenesis through a different mechanism that may involve sympathetic stimulation (Orava et al., 2011; Stanford et al., 2013). Indeed, an alternative role of macrophages in controlling thermogenesis involves their adhesion to sympathetic neurons that innervate thermogenic adipose depots (Wolf et al., 2017) and their capacity to degrade NE during aging and in obesity (Camell et al., 2017; Pirzgalska et al., 2017). Although we identified defective macrophage glutaminolysis as a critical regulator of the sympathetic tone of thermogenic adipose depots, we did not observe perturbations in the sympathetic innervation of BAT or NE degradation by sympathetic neuron-associated macrophages. Instead, we identified that macrophage glutaminolysis controls the sympathetic tone of thermogenic adipose depots by potentializing the glutamatergic neural pathway stemming from the IML region of the spinal cord located between the T2 and T6 segments, which is known to activate nonshivering thermogenesis under behavioral stress (Morrison and Madden, 2014; Tupone et al., 2014). Thus, our study identified an unprecedented and unexpected role of macrophage glutaminolysis in controlling spinal cord neuron activation required for sympathetic tone-dependent thermogenesis.

Although brain macrophages (i.e., microglia) and intestinal muscularis macrophages are known to communicate with neurons and control their activity (Crotti and Ransohoff, 2016; Muller et al., 2014), reports of interactions between macrophages and spinal nerves are scarce, and their relevance to metabolic function has not yet been investigated. Recent reports have identified populations of nerve-associated macrophages in different body regions and have suggested that these cells exhibit specific transcriptomic profiles depending on the nerve they communicate with (Wang et al., 2020; Ydens et al., 2020). Whether these diverse populations share common metabolic configurations and requirements, particularly the involvement of glutaminolysis, remains to be elucidated. Here, we documented a population of spinal cord macrophages that are present in the IML region of the gray matter, where spinal nerves, especially glutamatergic axons, normally unite. Transcriptomic analysis revealed that these macrophages were significantly distinct from brain microglia in terms of transcriptional machinery and were strongly impacted by defective glutaminolysis, consistent with earlier reports showing that they express lower levels of CD45 (Goldmann et al., 2016) and are metabolically more active than microglia (Zhu et al., 2017). These findings are consistent with divergent gene expression landscapes across different tissue-resident macrophages, supporting the idea of local macrophage adaptation (Gautier et al., 2012; Gosselin et al., 2014; Lavin et al., 2014; Okabe and Medzhitov, 2014). Spinal cord macrophage pseudopodia extending over axons are also morphologically distinct from the finely branching ramifications of brain microglia (Crotti and Ransohoff, 2016), which could offer an explanation for how glutaminolysis impacts these cells. Indeed, our results clearly demonstrated that the transcriptional profiles of spinal cord macrophages were modulated in Mac$^{\Delta Gls1}$ mice; specifically, the expression of genes involved in cell projection and the response to various stimuli was decreased, and the expression of genes associated with the microtubule cytoskeleton and mitochondrion rearrangement was increased. There was no evidence that these cells exhibited a proinflammatory profile. Among the modulated genes, members of the semaphorin and plexin families (i.e., *Sema3g* and *Plxnb3*), which are known to contribute to axonal guidance in the spinal cord (Ducuing et al., 2019), and various genes involved in cilium

and dendrite formation and movement (i.e., *Wdr78*, *Kctd17*, *Syt3*, *Tmem67*, *Plekha8* or *Rhof*), were identified; the changes in these genes require further exploration. Nevertheless, our data clearly revealed altered spindle-shaped spinal cord macrophages in the spinal cords of $Mac^{\Delta Gls1}$ mice, which affected autonomous medullospinal axonal activity, which is critical for sympathetic tone-dependent nonshivering thermogenesis (Morrison and Madden, 2014; Tupone et al., 2014) and metabolic adaptation of thermogenic brown adipose tissue (Chechi et al., 2013).

Collectively, our data reveal that macrophage glutaminolysis acts as a central component of metabolic adaptation at steady state and in HFD-induced obesity through two independent but complementary tissue-dependent roles. First, macrophage glutaminolysis limits visceral fat inflammation and storage in HFD-induced obesity. Second, we identified a previously unknown glutamine-dependent homeostatic role for spinal cord macrophages through which they control medullispinal glutamatergic transmission, favoring sympathetic tone activation in thermogenic adipose depots and glucose homeostasis. Overall, our study helps to elucidate the role of macrophage glutaminolysis in metabolic health and disease.

Figure 1

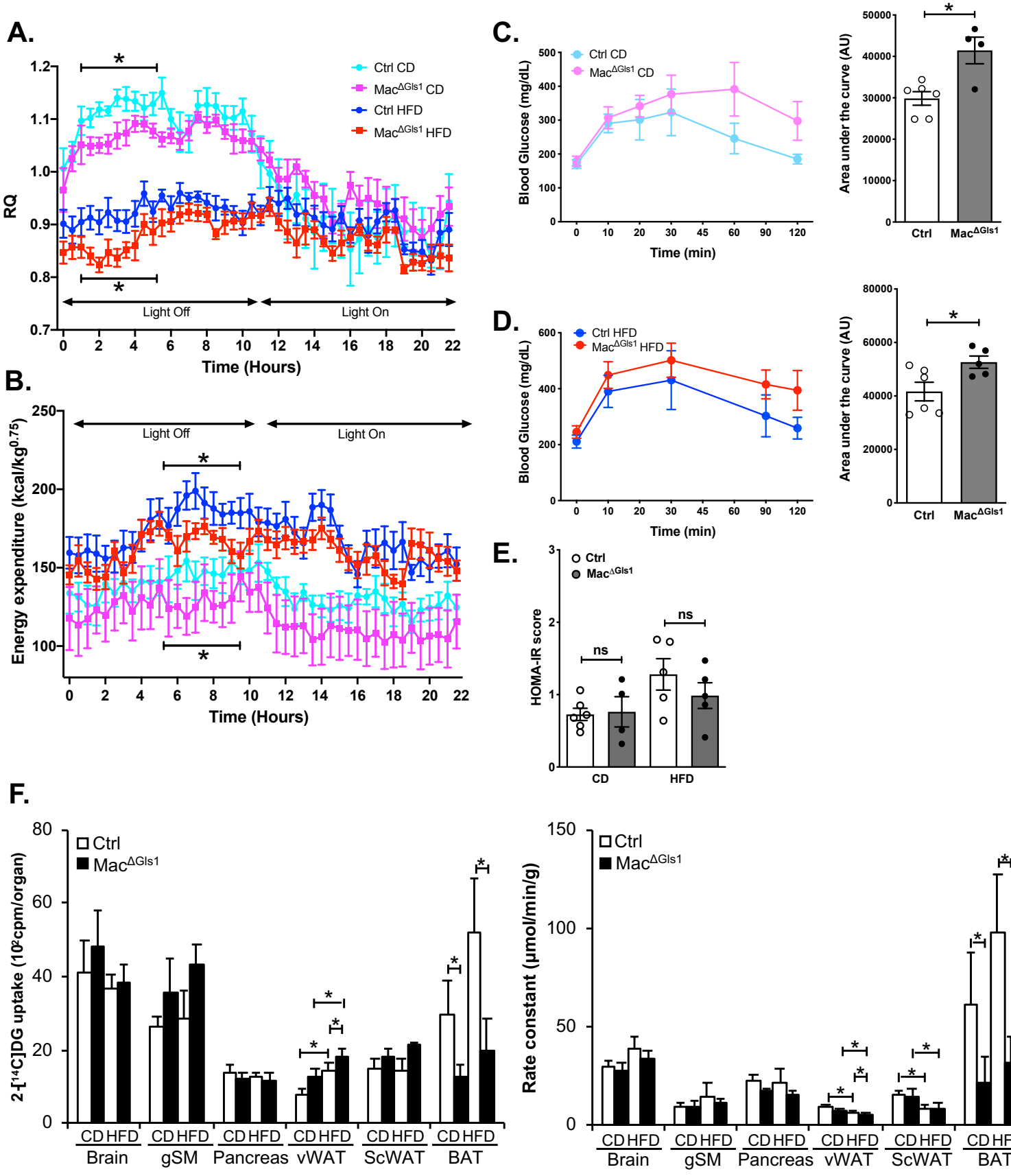
A.
RQ
Time (Hours)
Ctrl CD
Mac$^{\Delta Gls1}$ CD
Ctrl HFD
Mac$^{\Delta Gls1}$ HFD
Light Off
Light On
B.
Energy expenditure (kcal/kg$^{0.75}$)
Time (Hours)
Light Off
Light On
C.
Blood Glucose (mg/dL)
Time (min)
Ctrl CD
Mac$^{\Delta Gls1}$ CD
Area under the curve (AU)
Ctrl
Mac$^{\Delta Gls1}$
D.
Blood Glucose (mg/dL)
Time (min)
Ctrl HFD
Mac$^{\Delta Gls1}$ HFD
Area under the curve (AU)
Ctrl
Mac$^{\Delta Gls1}$
E.
HOMA-IR score
Ctrl
Mac$^{\Delta Gls1}$
ns
CD
HFD
F.
2-[^{14}C]DG uptake (10^{2}cpm/organ)
Ctrl
Mac$^{\Delta Gls1}$
CD HFD
Brain
gSM
Pancreas
vWAT
ScWAT
BAT
Rate constant (µmol/min/g)

Figure 1. Macrophage Gls1 deficiency reduces glucose utilization independently of visceral fat inflammation. **(A)** Respiratory quotient and **(B)** whole-body energy expenditure measured by indirect calorimetry in control and Gls1 deficient mice ($Mac^{\Delta Gls1}$) fed for 12 weeks with a standard chow or high-fat diet (CD and HFD, respectively). **(C)** Intraperitoneal glucose tolerance test (ipGTT) performed on fasted CD-fed and **(D)** HFD-fed control and $Mac^{\Delta Gls1}$ mice. Blood glucose concentrations were measured at the indicated time points. Quantifications are calculated as the glucose area under the curve (AUC). **(E)** Insulin resistance index in control and $Mac^{\Delta Gls1}$ mice fed for 12 weeks with a CD or HFD. The insulin resistance index is calculated as fasting insulin x fasting blood glucose/405 and expressed as HOMA-IR score. **(F)** Tissue uptake (left panel) and rate constant (right panel) of 2-[^{14}C]-deoxyglucose (2-[^{14}C]-DG) in CD and HFD-fed control and $Mac^{\Delta Gls1}$ mice (40min after *i.v.* injection of the radiolabeled tracer). All values are means ± SEM and are representative of an experiment of five to seven animals per group. *, $P<0.05$ versus control.

Figure 2

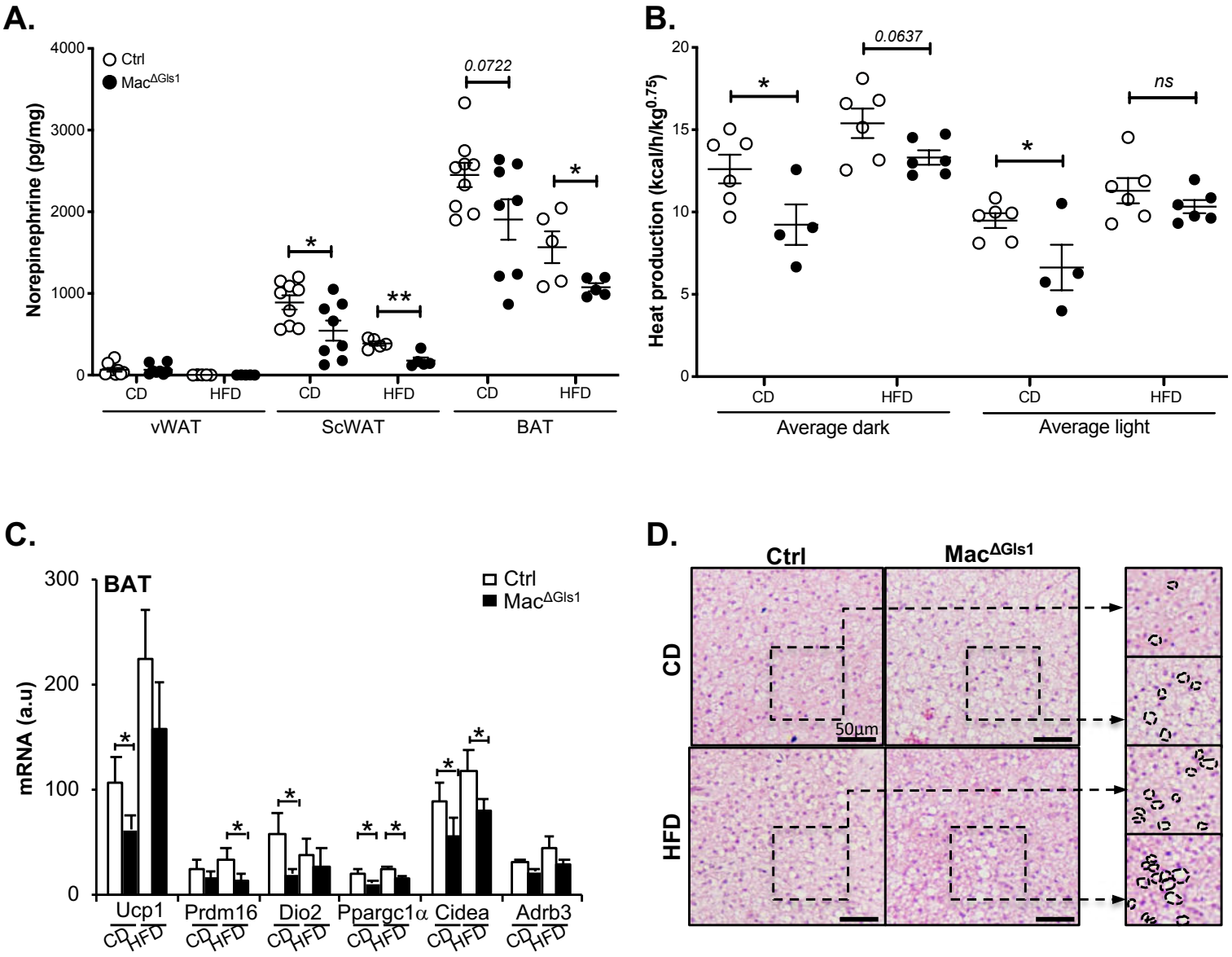

Figure 2. Macrophage-restricted deletion of Gls1 reduces catecholamine levels in thermogenic adipose depots and impairs BAT-dependent thermoregulation. (A) Norepinephrine (NE) levels in visceral and thermogenic adipose tissues of CD and HFD-fed control and Mac$^{\Delta Gls1}$ mice; each dot represents one animal. **(B)** Heat production in these mice calculated by indirect calorimetry and presented as the average values for the light or dark periods during the final 24h of monitoring; each symbol represents an individual mouse. **(C)** Expression of genes encoding molecules involved in thermogenesis in BAT of CD and HFD-fed control and Mac$^{\Delta Gls1}$ mice, assessed by RT-qPCR. **(D)** Histology of hematoxylin- and eosin (H&E)-stained BAT from CD and HFD-fed Mac$^{\Delta Gls1}$ mice and their littermates at the end of the study period. All values are means ± SEM and are representative of at least one experiment (n= 5-9). *, *P*<0.05 versus control.

Figure 3

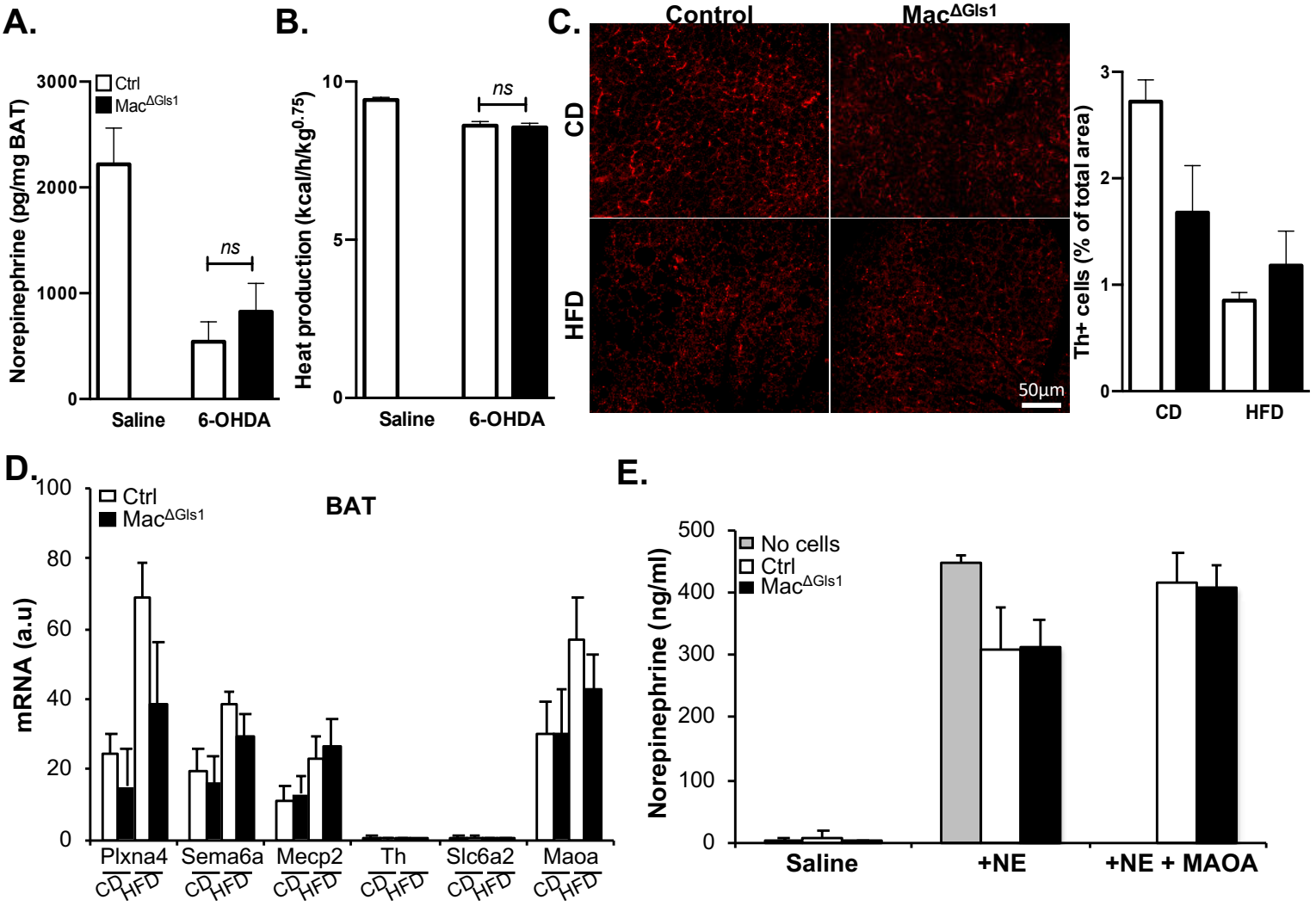

Figure 3. Defective macrophage glutaminolysis impacts the sympathetic tone but does not diminish BAT innervation or NE degradation. Effect of neurochemical sympathectomy of control and Mac$^{\Delta Gls1}$ mice with 6-hydroxydopamine (6-OHDA) on **(A)** BAT NE levels and **(B)** heat production calculated by indirect calorimetry. **(C)** Visualization of tyrosine hydroxylase (Th)$^{+}$ fibers by immunofluorescence microscopy in BAT of CD and HFD-fed control and Mac$^{\Delta Gls1}$ mice. **(D)** RT-qPCR analysis of genes involved in the repulsion of neurons or NE degradation in BAT of CD and HFD-fed control or Mac$^{\Delta Gls1}$ mice. **(E)** NE content in the media of cell-sorted sympathetic neuron-associated macrophages (SAMs) cultured overnight in presence or absence of NE and chlorgyline, a MAOA blocker. All values are means ± SEM and are representative of an experiment of five to seven animals per group. *, P<0.05 versus control.

Figure 4

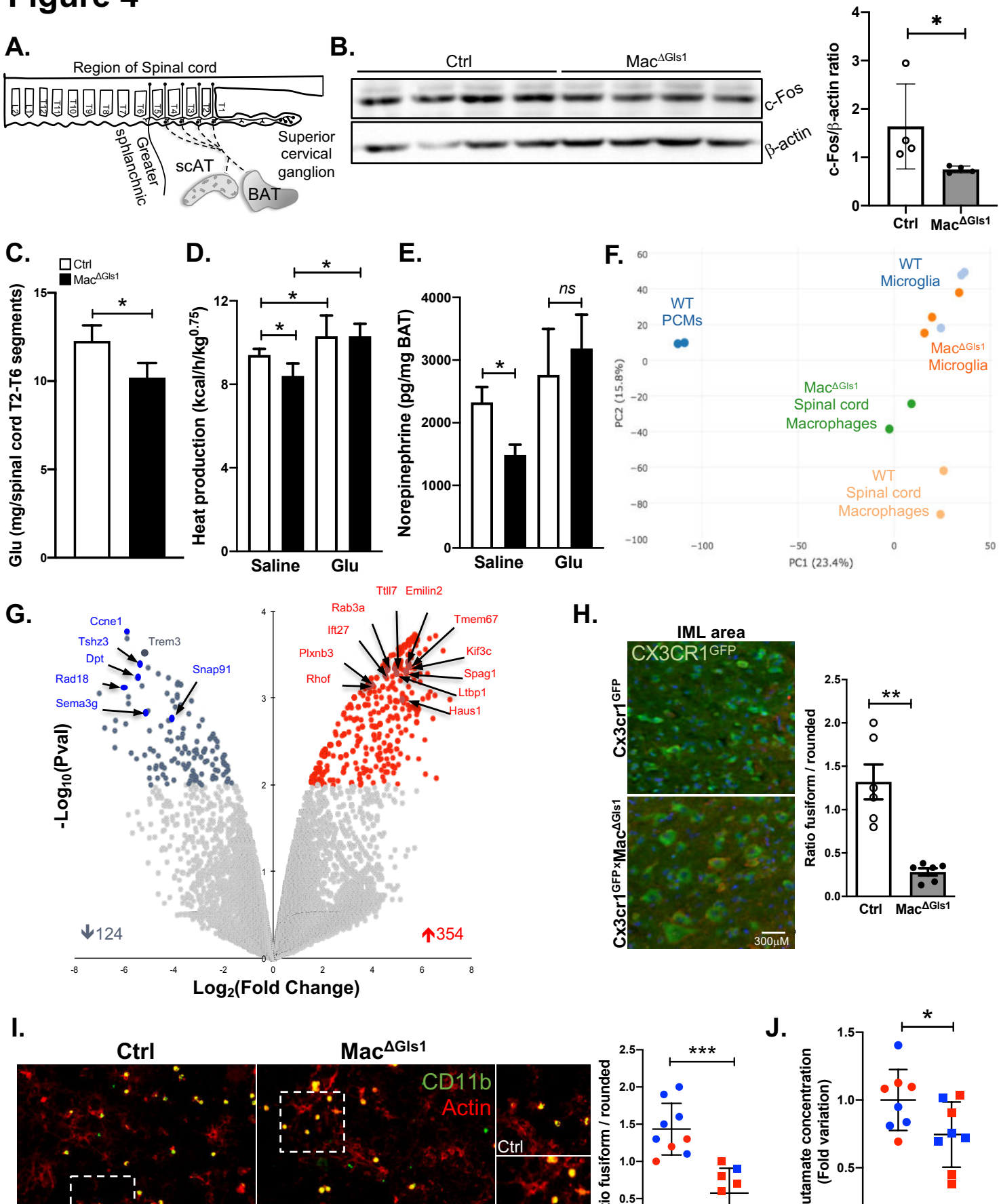
A.
Region of Spinal cord
Greater splanchnic
scAT
BAT
Superior cervical ganglion
B.
Ctrl
Mac^ΔGls1
c-Fos
β-actin
c-Fos/β-actin ratio
C.
Glu (mg/spinal cord T2-T6 segments)
D.
Heat production (kcal/h/kg^0.75)
Saline
Glu
E.
Norepinephrine (pg/mg BAT)
ns
F.
WT PCMs
WT Microglia
Mac^ΔGls1 Microglia
Mac^ΔGls1 Spinal cord Macrophages
WT Spinal cord Macrophages
PC1 (23.4%)
PC2 (15.8%)
G.
Ccne1
Tshz3
Trem3
Dpt
Rad18
Snap91
Sema3g
Ttll7
Emilin2
Rab3a
Ift27
Tmem67
Plxnb3
Kif3c
Rhof
Spag1
Ltbp1
Haus1
-Log10(Pval)
↓124
↑354
Log2(Fold Change)
H.
IML area
CX3CR1^GFP
Cx3cr1^GFP
Cx3cr1^GFP×Mac^ΔGls1
300μM
Ratio fusiform / rounded
I.
Ctrl
Mac^ΔGls1
CD11b
Actin
50μM
J.
Glutamate concentration (Fold variation)

Figure 4. Identification and characterization of a role for glutaminolysis in spinal cord macrophages. (A) Schematic illustration showing the sympathetic innervation of thermogenic adipose tissues stemming from the IML region of the spinal cord located between T2 and T6 segments. **(B)** Immunoblot of c-Fos and β-actin of spinal cord T2-T6 segments. The bar graph show densitometry quantification of immunoblots normalized to β-actin. **(C)** Glutamate levels in the spinal cord T2-6 segments of control or $Mac^{\Delta Gls1}$ mice. **(D)** Effect of glutamate supplementation (50mg/kg for 12 days) in control and $Mac^{\Delta Gls1}$ mice on heat production calculated by indirect calorimetry and **(E)** BAT NE levels. **(F)** PCA based on gene expression from RNA-seq of cell sorted control PCMs (blue), control and Gls1-deficient microglia (light blue and orange, respectively) and control and Gls1-deficient spinal cord macrophages (green and light orange, respectively). Each dot represents an independent experiment. **(G)** Volcano plot shows genes differentially expressed between control and Gls1-deficient spinal cord macrophages with differences in expression (*P* value ($-\log_{10}$)) plotted against $\log_2$-fold change (based on RNA-seq data). Genes with significantly different expression (a *P* value of < 0.01) in Gls1-deficient spinal cord macrophages were indicated in red (upregulation) or in blue (downregulation). **(H)** Confocal microscopy of the intermediolateral cell column (IML) of the spinal cord isolated from $CX3CR1^{gfp/+}$ or $CX3CR1^{gfp/+}$ $Mac^{\Delta Gls1}$ mice and quantification of the ratio of fusiform/rounded macrophages. Cells were counterstained with DAPI (nuclear staining). Each dot represents a cell from pooled animals. **(I)** Primary neocortical cultures, enriched in glutamatergic neurons, were incubated for 16 h with PCMs (blue) or cell-sorted spinal cord macrophages (red) and visualized by immunofluorescence microscopy of actin and CD11b (left panel). Spindle-shaped macrophages (i.e., fusiform/rounded ratio) were quantified (right panel). **(J)** Glutamate levels in media, a hallmark of glutamatergic neuron activation, were also quantified. Each dot represents an experiment from an individual mouse. All values are means ± SEM and are representative of an experiment of up to five animals per group. *, *P*<0.05 versus control. **, *P*<0.01 versus control. ***, *P*<0.001 versus control.

Table S1. Effect of Gls1 deficiency on energy metabolism.

	Chow diet			High fat diet		
	Control	**Mac$^{\Delta Gls1}$**	***P***	**Control**	**Mac$^{\Delta Gls1}$**	*P*
Food intake (kcal/day)	17.91±0.76	14.89±1.30	*	19.34±3.65	17.66±3.91	*NS*
EE (kcal/day/kg$^{0.75}$)	135.1±3.1	118.2±3.3	***	171.0±2.2	160.7±1.6	***
Gox (kcal/day/kg$^{0.75}$)	116.6±4.7	95.7±5.3	*	121.8±4.1	93.4±3.5	***
Lox (kcal/day/kg$^{0.75}$)	18.5±1.5	22.5±0.8	*NS*	49.2±2.5	67.2±2.9	***
Locomotor activity (a.u)	109.2±8.4	94.9±7.2	*NS*	72.6±6.3	81.2±6.8	*NS*

Indirect calorimetry parameters (food intake, energy expenditure (EE), glucose oxidation (Gox), lipid oxidation (Lox) and locomotor activity) of control and Mac$^{\Delta Gls1}$ mice fed on CD or HFD for 12 weeks. Data are means ± SEM (n=5-7 per group). *, $P<0.05$; ***, $P<0.001$ versus control.

Supplemental Figure 1

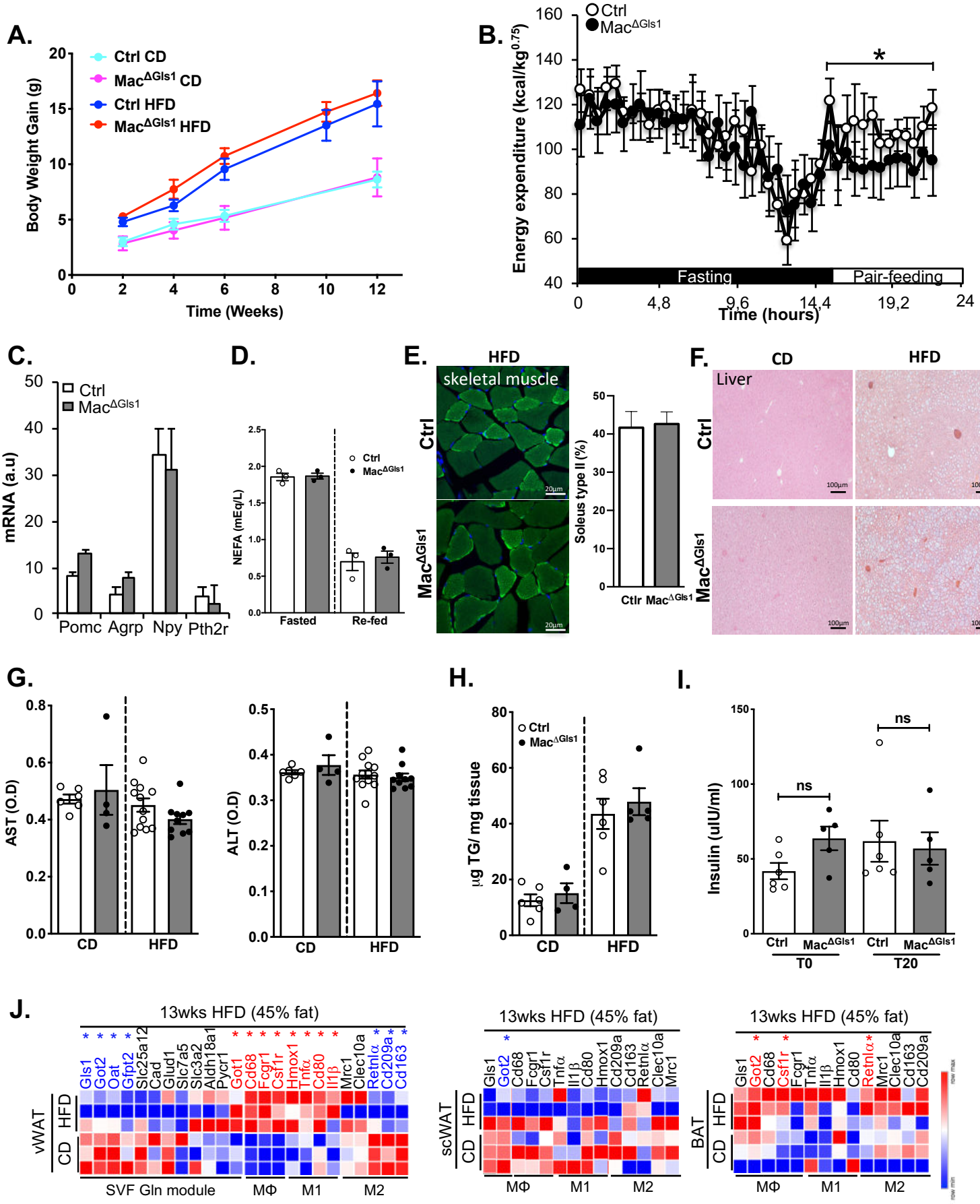

Supplemental Figure 1

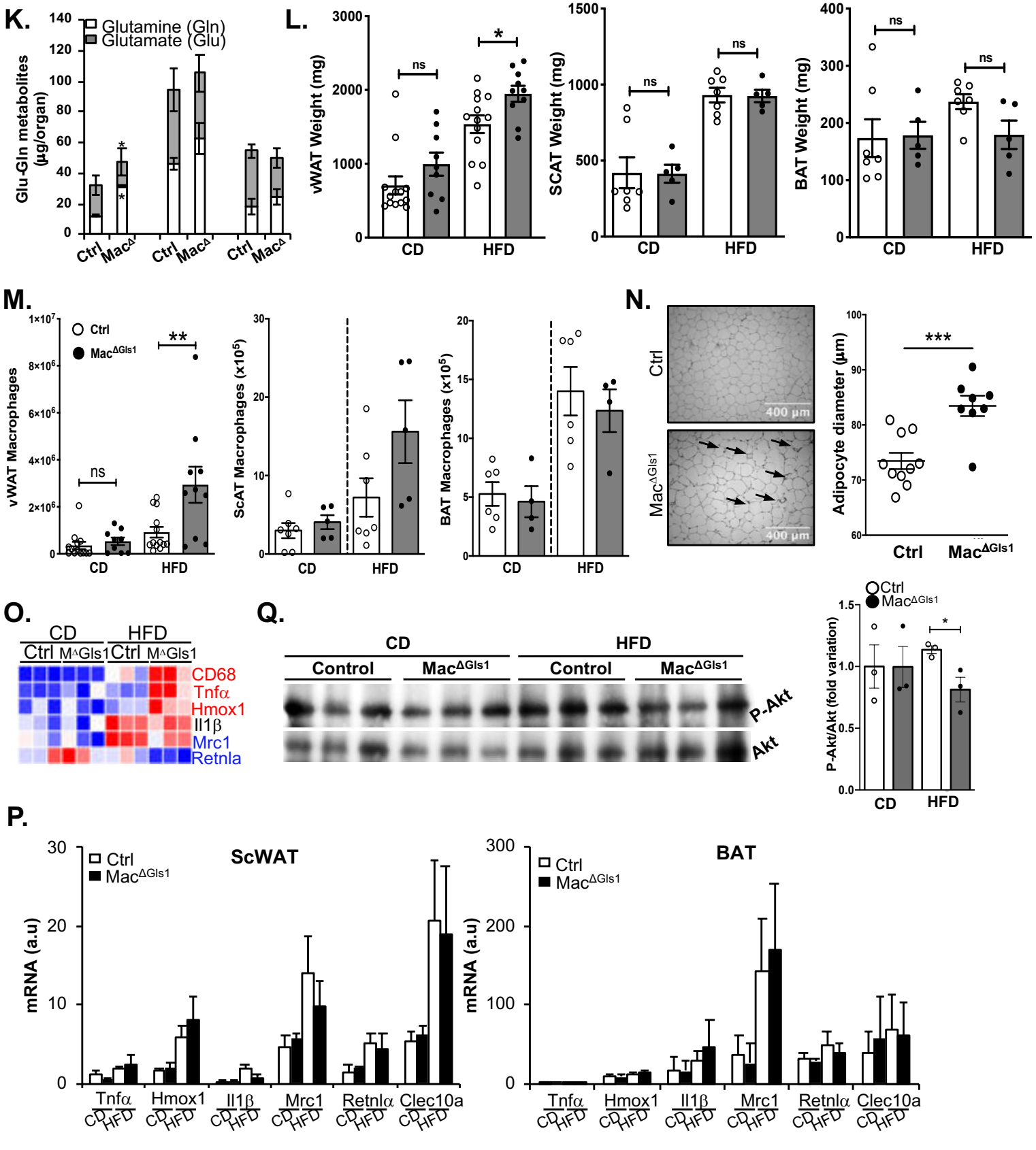

Figure S1. Effect of macrophage glutaminolysis deficiency on metabolic and adipose tissue parameters. (A) Body weight gain of control and Mac$^{\Delta Gls1}$ mice fed a CD or HFD for 12 weeks. **(B)** Whole-body energy expenditure of control and Mac$^{\Delta Gls1}$ mice subjected to fasting and pair-feeding. **(C)** RT-qPCR analysis of genes encoding central feeding regulatory neuropeptides in hypothalami obtained from CD fed control and Mac$^{\Delta Gls1}$ mice. **(D)** Plasma non-esterified fatty acid (NEFA) levels in mice of the indicated genotypes. **(E)** Representative sections of gastrocnemius skeletal muscle immunostained with antibodies against type II MyHC to visualize type II oxidative fibers in HFD-fed control and Mac$^{\Delta Gls1}$ mice. **(F)** Representative H&E staining of liver sections of CD or HFD-fed control and Mac$^{\Delta Gls1}$ mice. Effect of Gls1 deficiency on **(G)** plasma AST and ALT levels and **(H)** liver triglyceride content in mice of the indicated genotypes. **(I)** Plasma insulin concentrations during the ipGTT at time 0 and 20min in HFD-fed control and Mac$^{\Delta Gls1}$ mice. **(J)** Microarray analysis of vWAT, ScWAT and BAT isolated from CD and HFD-fed WT mice (GSE28440) and heatmaps were performed with Phantasus software. Genes labeled in red are significantly upregulated and genes labeled in blue are significantly downregulated. **(K)** Glutamine and glutamate concentrations in adipose depots of CD-fed control or Mac$^{\Delta Gls1}$ mice. **(L)** Weight of different adipose depots (vWAT, ScWAT and BAT) in CD or HFD-fed control and Mac$^{\Delta Gls1}$ mice. Each dot represents one animal. **(M)** Quantification of macrophage numbers in vWAT, ScWAT and BAT analyzed by flow cytometry. Each dot represents one animal. **(N)** Representative H&E staining of vWAT sections and quantification of adipocyte diameter in HFD-fed control and Mac$^{\Delta Gls1}$ mice. **(O)** Expression of anti- and pro-inflammatory genes in the vWAT of CD and HFD-fed control and Mac$^{\Delta Gls1}$ mice, assessed by qPCR. **(P)** RT-qPCR analysis of anti and pro-inflammatory genes in the ScWAT and BAT of the indicated genotypes. **(Q)** Western blot analysis of phospho-Akt and total Akt in the vWAT of CD and HFD-fed control and Mac$^{\Delta Gls1}$ mice. All values are means ± SEM and are representative of an experiment of five to seven animals per group. *, $P<0.05$; **, $P<0.01$; ***, $P<0.001$ versus control.

Supplemental Figure 2

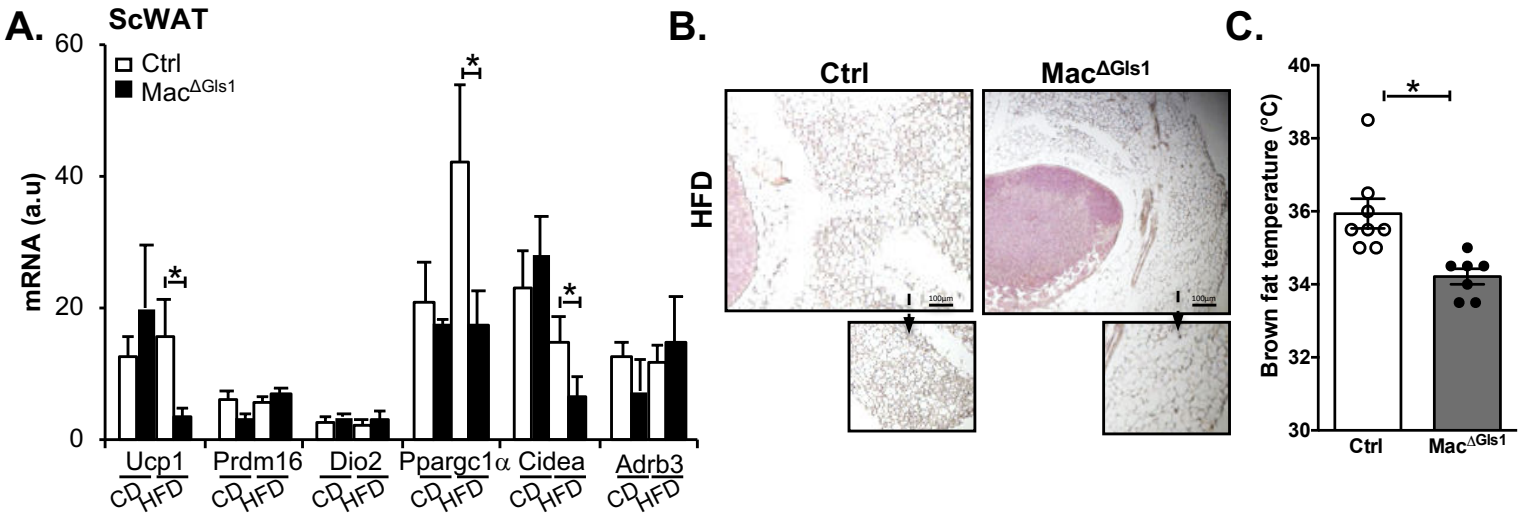

Figure S2. Macrophage Gls1 deficiency causes impairment of ScWAT browning. (A) Expression of genes encoding molecules involved in thermogenesis in ScWAT of CD and HFD-fed control and Mac$^{\Delta Gls1}$ mice, assessed by RT-qPCR. **(B)** Representative H&E staining of ScWAT sections showing clusters of multilocular or unilocular brown fat-like in HFD-fed control or Mac$^{\Delta Gls1}$ mice. **(C)** Changes in BAT temperature in the absence of Gls1 in macrophages. All values are means ± SEM and are representative of at least one experiment (n= 5-9). *, *P*<0.05 versus control.

Supplemental Figure 3

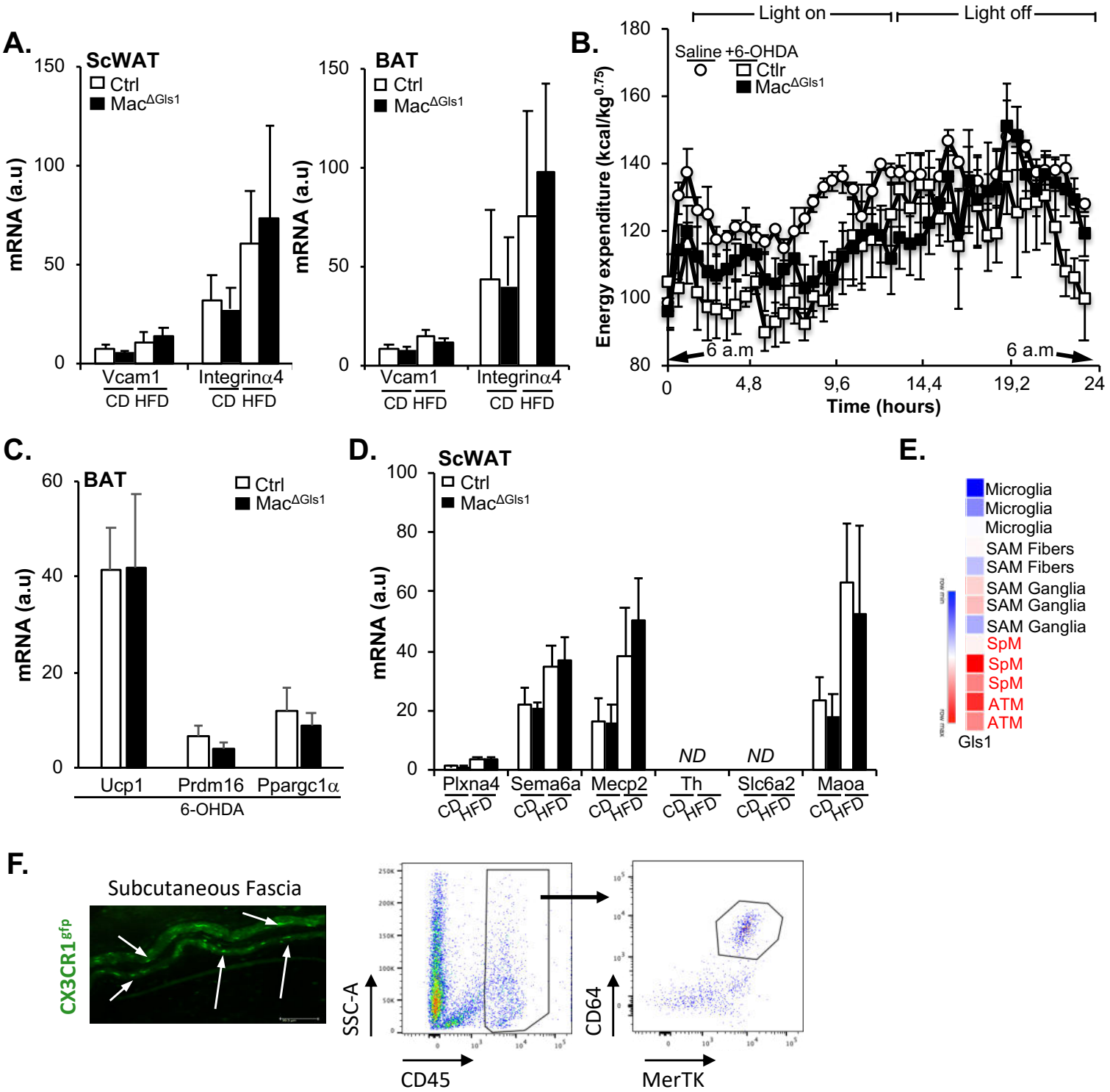

Figure S3. Effect of macrophage glutaminolysis on cell adhesion molecule-dependent browning and its dependence on sympathetic tone. (A) RT-qPCR analysis of genes involved in macrophage-adipocyte adhesion in ScWAT and BAT of CD and HFD-fed control or $Mac^{\Delta Gls1}$ mice. Effect of neurochemical sympathectomy of control and $Mac^{\Delta Gls1}$ mice with 6-hydroxydopamine (6-OHDA) on **(B)** whole-body energy expenditure measured by indirect calorimetry and **(C)** expression of genes encoding molecules involved in BAT thermogenesis assessed by RT-qPCR. **(D)** RT-qPCR analysis of genes involved in the repulsion of neurons or NE degradation in ScWAT of CD and HFD-fed control or $Mac^{\Delta Gls1}$ mice. **(E)** Comparative analysis of Gls1 expression in different macrophage populations from a publicly available dataset (GSE103847). **(F)** Visualization of sympathetic neuron-associated macrophages (SAMs) in the subcutaneous fascia of $CX3CR1^{gfp/+}$ mice (left) and flow cytometry gating strategy for isolation (right). All values are means ± SEM and are representative of an experiment of five to seven animals per group.

Supplemental Figure 4

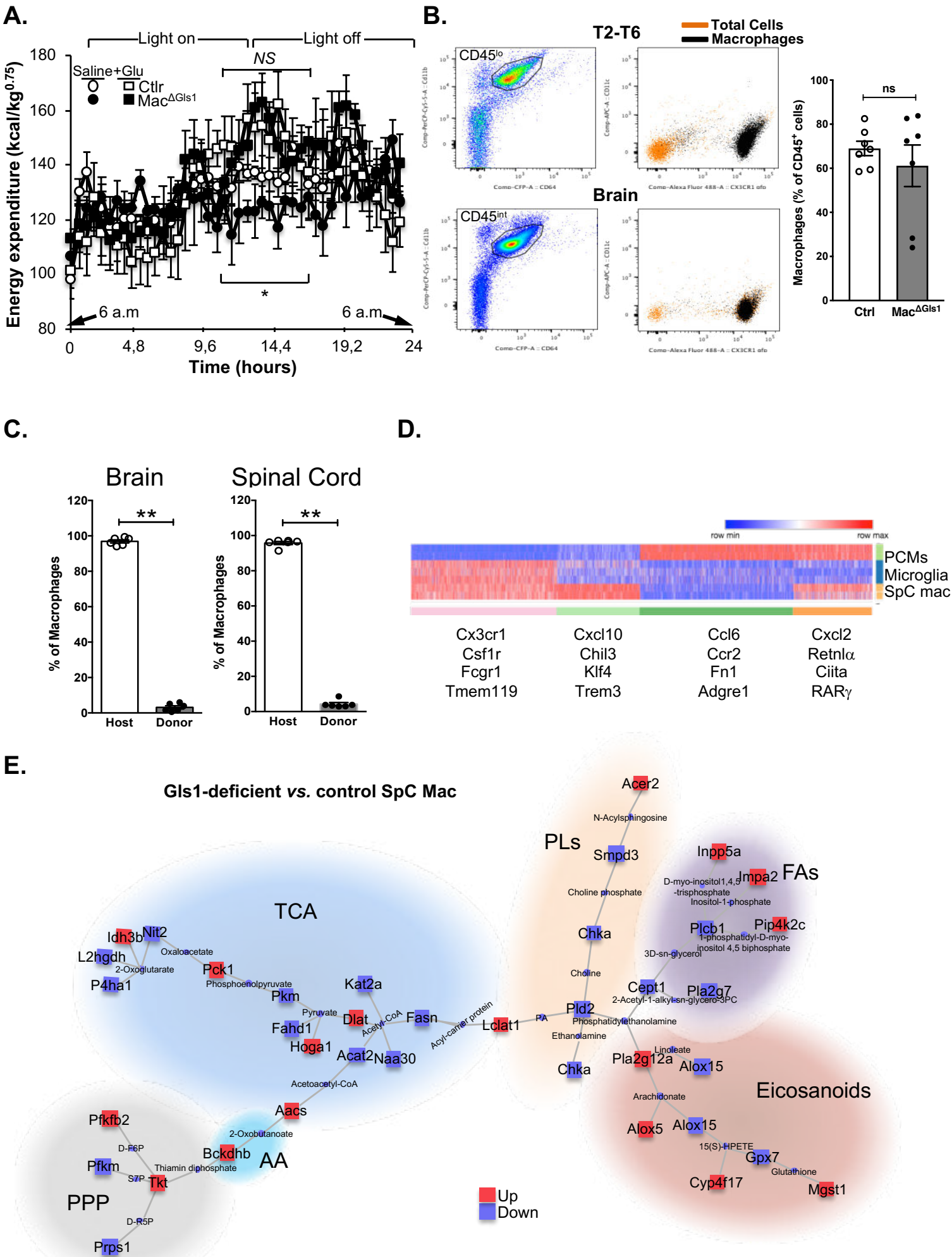

Supplemental Figure 4

F.

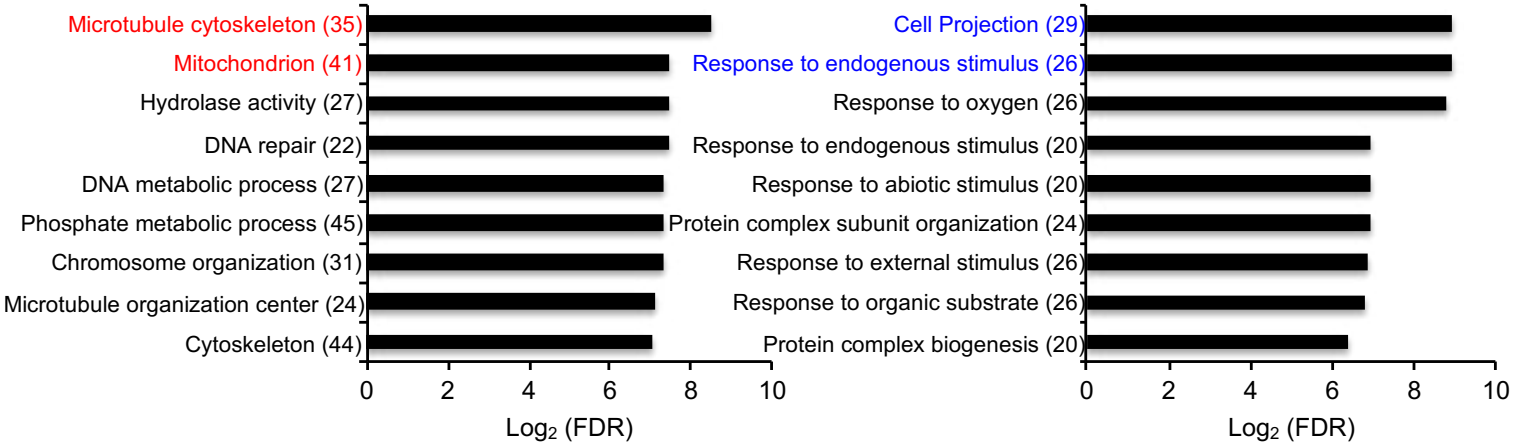

G.

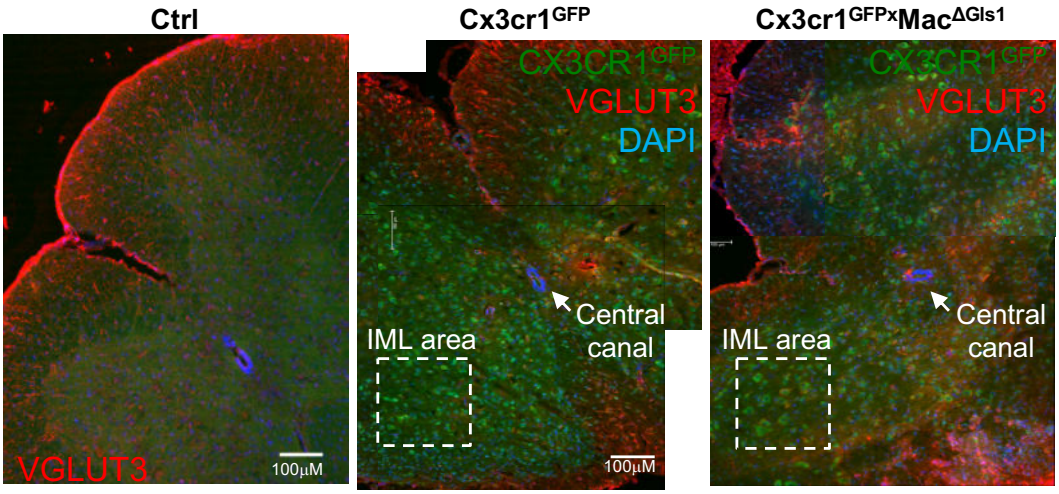

Figure S4. Characterization of Gls1-deficient spinal cord macrophages. (A) Effect of glutamate supplementation on whole-body energy expenditure measured by indirect calorimetry in control and Mac$^{\Delta Gls1}$ mice. **(B)** Gating strategy of brain microglia and spinal cord macrophages by flow cytometry. **(C)** Repopulation experiment after CX3CR1$^{gfp/+}$ (CD45.1) bone marrow transplantation into lethally irradiated CD45.2 control recipients and quantification of the percentage of repopulating microglia (left) and spinal cord macrophages (right) by flow cytometry. **(D)** K-means clustering of genes associated with PCMs, microglia and spinal cord macrophages from RNA-seq dataset of control mice. **(E)** Metabolic pathway analysis from RNAseq data of control and Mac$^{\Delta Gls1}$ spinal cord macrophages using CoMBI-T topological tool. **(F)** Functional annotation enrichment analysis for GO terms from RNAseq analysis of control and Gls1-deficient spinal cord macrophages (upregulated pathway in left panel and downregulated pathway in right panel). **(G)** Confocal microscopy of spinal cord isolated from CX3CR1$^{gfp/+}$ or CX3CR1$^{gfp/+}$ Mac$^{\Delta Gls1}$ mice counterstained with VGLUT3 (spinal cord neuron staining) antibody and DAPI (nuclear staining). All values are means ± SEM and are representative of an experiment of five to seven animals per group. **, *P*<0.005 versus control.

Acknowledgments. We thank Dr Fréderic Labret for assistance with flow cytometry, Dr Véronique Corcelle and her team for assistance in animal facilities and Dr. Marie Irondelle for assistance with confocal microscopy (C3M Imaging Core Facility funded by the Conseil Général Alpes-Maritimes and Région PACA, which belongs to the IBISA Microscopy and Imaging platform Côte d'Azur (MICA). C3M biochemical and Seahorse analyzers were co-funded by the Conseil Général Alpes-Maritimes and Région PACA.

Financial support and sponsorship. This work was supported by grants from the Fondation de France (FDF), the National Agency for Research (ANR) and the European Research Council (ERC) consolidator program (ERC2016COG724838) to L.Y.C.

Disclosures. The authors have declared that no conflict of interest exists.

Author contributions.
L.Y.C conceived the project, designed the experiments and wrote the manuscript. J.M. and S.I. designed the experiments and performed most of the molecular, histological or *in vivo* experiments. M.A., N.V., J.G., K.D., M.O., R.G. helped with experimental design and assisted with data analysis. A.S. and M.N.A helped with bioinformatic data analysis. J.M., I.G.S., and S.R., provided tool materials for *in vivo* studies. M.C., J.F.T., D.B.R., E.L.G., R.G., and M.N.A provided scientific advice and helped with experimental design. L.Y.C. also designed and supervised the study and obtained funding. All authors read, edited, and approved the manuscript.

STAR Methods

Lead Contact and Materials Availability

Lead contact. Further information and requests for resources and reagents should be directed to and will be fulfilled by the Lead Contact, Dr. Laurent Yvan-Charvet (yvancharvet@unice.fr).

Experimental model and subject details

Mice. $Gls1^{fl/fl}$ mice were kindly provided by Pr. Stephen Rayport's lab and have been crossed to $Lyz2^{Cre}$ mice (B6.129P2-Lyz2tm1(cre)Ifo/J, The Jackson Laboratory) and $CX3CR1^{gfp}$ [B6.129P-$Cx3cr1^{tm1Litt}$/J, The Jackson Laboratory) mice. For each experiment, co-housed littermate controls were used. Animal protocols were approved by the Institutional Animal Care and Use Committee of the French Ministry of Higher Education and Research and the Mediterranean Center of Molecular Medicine (Inserm U1065) and were undertaken in accordance with the European Guidelines for Care and Use of Experimental Animals. Animals had free access to food and water and were housed in a controlled environment with a 12-hour light–dark cycle and constant temperature (22°C). Obesity was induced by feeding the mice with a Western diet (TD88137, Ssniff) for 12 weeks. Mice were weighted every two weeks following Western diet induction.

Peritoneal cavity macrophage (PCM) culture. Resident PCMs were obtained by PBS lavage of the peritoneal cavity and macrophages were enriched by 2hour incubation in 96-well flat bottom plates. Cells were then washed 3 times and adherent cells were cultured overnight in complete RPMI 1640 medium (Corning) containing 10mM glucose, 2mM L-glutamine, 100U/ml penicillin/streptomycin, and 10% FBS at 37°C and 5% CO2.

Sympathetic neuron-associated macrophage (SAM) culture. Subcutaneous fascia was carefully excised and digested with collagenase A (1,5mg/ml) for 30minutes. Red blood cells were then lysed, and macrophages enriched by 2hour incubation in 96-well flat bottom plates. Cells were then washed 3 times and adherent cells were cultured overnight in complete RPMI 1640 medium (Corning) containing 10mM glucose, 2mM L-glutamine, 100U/ml penicillin/streptomycin, and 10% FBS at 37°C and 5% CO2.

Brain dissection and cortical neuron dissociation. As previously published (Marcuzzo et al., 2019), whole brains were extracted from P18 mouse embryos and placed in a dissociation medium containing 134 mM Na-isethionate, 2 mM KCl, 8 mM MgCl, 100 µM CaCl2, 23 mM D-glucose, 15 mM Hepes and 1 mM kynurenic acid, pH 7.2. Working with tweezers under a dissection microscope, the hemispheres were carefully separated; the cerebellum, septum, thalamus and hypothalamus were separated from the cortex, followed by the meninges and hippocampus. The cortices were cut into 1-mm3 pieces, digested in XIV protease for 20 min at 37 °C by gentle agitation, and washed with dissociation medium at room temperature three times. The pieces were subsequently mechanically homogenized using fire-polished Pasteur pipettes having three decreasing diameter sizes, and the resulting supernatant containing neurons was collected into a new tube (Hilgenberg and Smith, 2007, Cestèle et al., 2008). The neurons were maintained in a culture medium containing Neurobasal A, 0.5% glutamax, 0.5% penicillin/streptomycin, 2% B27, 10 µg/ml fibroblast growth factor (Thermo Fisher Scientific Inc., Foster City MA, USA) until 28 DIV.

Method details

Mice and treatments. For the glutamate supplementation experiment, mice were *i.p.* injected with 50mg/Kg for 12 consecutive days. For the chemical denervation experiment, mice were subcutaneously injected every 2 days for a week with 10mg/mL of 6-hydroxydopamine (6-OHDA).

Bone marrow transplantation. Bone marrow transplantation was performed as previously described (Gautier et al., 2013). Briefly, WT (CD45.2) and Cx3cr1^{GFP} (CD45.1) were lethally irradiated 16h before transplantation. Then, WT recipient mice were *i.v.* injected with BM from Cx3cr1^{GFP} mice and Cx3cr1^{GFP} recipients were *i.v.* injected with BM from WT mice. Mice were then allowed to recover for five weeks before sacrifice and analysis.

Calorimetry. *In vivo* indirect open circuit calorimetry was performed in metabolic chambers using the Labmaster system (TSE-Systems, Bad Homburg, Germany). The 12-week-old animals were randomly and alternatively placed into experimental chambers at 25°C ± 1 with free access to food and water. Constant airflow (0.5 l/min) was drawn through the chamber and monitored by a mass-sensitive flowmeter. To calculate oxygen consumption (VO_2), carbon dioxide production (VCO_2), and respiratory quotient (RQ: ratio of VCO_2 to VO_2), gas concentrations were monitored at the inlet and outlet of the scaled chambers. Data were collected after 24 hours of adaptation in acclimated singly housed mice. Total metabolic rate (energy expenditure) was calculated from oxygen consumption and carbon dioxide production using Lusk's equation and expressed as watts per kilogram to the 0.75 power of body weight. Glucose, lipid oxidation and heat production were calculated as previously described (Gautier et al., 2013)(Wolf et al., 2017).

Glucose Tolerance Test. Mice were fasted for 6 hours and then injected i.p. with D-Glucose (2g/kg of body weight). Blood samples were collected at different times by tail bleeding after injection (Gautier et al., 2013). Blood glucose was measured with Optium Xceed Glucometer (Abbott). Graphical representations were generated using GraphPad Prism 7 and the area under the curve for each animal was calculated. Blood samples were also collected at time 0 and 20 minutes to determine serum insulin levels using Insulin Mouse Serum Assay kit (Cisbio, PerkinElmer) according to the manufacturer's instructions.

Homeostasis Model Assessment of Insulin Restistance scores. The homeostasis model assessment of insulin resistance (HOMA-IR) scores were calculated from glucose and insulin concentrations obtained from mice after 6 h of fasting. The following equation was used: fasting insulin (ng/mL) x fasting blood glucose (mg/dL)/405.

***In vivo* 2-[^{14}C]-DG uptake.** Uptake of 2-[^{14}C]-DG in peripheral tissues was measured as previously described (Gautier et al., 2013). In brief, 2 µCi 2-[^{14}C]-DG was *i.v.* injected, and blood samples were collected at 5, 10, 20, 30, and 40 min. Blood glucose was monitored through the study period with a glucometer (Roche). After 40 min, brain, skeletal muscle, pancreas and adipose tissues were rapidly dissected, weighed, and homogenized with 5% $HClO_4$ solution. The radioactivity incorporated in both 2-[^{14}C]-DG and its 6-phosphate derivative was measured in the $HClO_4$ extract and expressed as total radioactivity per tissue weight. The rate constant of net tissue uptake of 2-[^{14}C]-DG was also calculated. In brief, the relative glucose uptake was calculated by dividing the area under the blood 2-[^{14}C]-DG disappearance curve (cpm/min/ml) to the steady-state glucose concentration (mM) multiplied by the tissue 2-[^{14}C]-DG (cpm/g tissue or cpm/10^6 cells for the BM) at 40 min.

Western Blotting. BM cells were harvested from mouse femur and tibia and differentiated in the presence of recombinant mouse M-CSF (20 ng/ml; Miltenyi) in complete RPMI 1640 medium (Corning) containing 10mM glucose, 2mM L-glutamine, 100U/ml of penicillin/streptomycin, and 10% FBS for 7 days at 37°C and 5% CO2. Cells were then lysed

in RIPA buffer containing protease inhibitors cocktail (ThermoFisher) and agitated for 1 hour at 4°C before centrifugation at 14000 rpm for 10min at 4°C. Supernatants were sampled and later used for SDS-PAGE. Protein content was evaluated using Pierce™ BCA assay kit (ThermoFisher). Protein samples were resolved on 10% SDS-PAGE gels and were then transferred onto polyvinylidene difluoride membrane using a wet transfer system. Membranes were blocked in 5% (w/v) BSA in Tris-buffered saline-Tween for one hour at room temperature. Membranes were then incubated with primary antibody (anti-cFos antibody (Abcam), anti Phospho-Akt antibody (Cell Signaling Technology) or anti-Akt antibody (Cell Signaling Technology)) followed by the appropriate horseradish peroxidase-conjugated secondary antibody. Anti α-actin mAb (Santa Cruz) was used as loading control. Proteins were detected by substrate HRP (Sigma).

Plasma biochemical parameters. Plasma multi-analyte profiling was performed using a clinical chemistry analyzer (Mindray BS-240 Pro, BioSentec) with the following colorimetric kits: NEFA-HR2 (Fujifilm Wako), triglycerides Reagent (Sigma) and alanine aminotransferase (ALT-0102) and aspartate aminotransferase (AST-0102), all from Biosentec.

Glutamine and glutamate measurements. Tissues were harvested and mechanically disrupted with mammalian ringer buffer solution (Electron Microscopy Sciences). Glutamine and glutamate concentrations were measured using YSI 2050 Biochemistry analyzer. To analyze glutamine and glutamate media content we used a commercially available Glutamine/Glutamate-GloTM Assay (Promega) in accordance with the manufacturer's instructions.

Norepinephrine measurement. Tissues were harvested and mechanically disrupted with mammalian ringer buffer solution (Electron Microscopy Sciences). Norepinephrine concentration was measured using Norepinephrine ELISA Kit (abnova) according to the manufacturer's instructions.

Norepinephrine degradation assay. Sympathetic neuron-associated macrophages **(**SAMs) were cell-sorted from subcutaneous fascia and incubated overnight with the following treatments: Norepinephrine (2µM, Abcam), Chlorgyline (100µM, Abcam). After an overnight incubation period, media were collected, and NE levels were quantified.

Macrophage-Neuron co-culture. We cultured primary neocortical neurons from P18 wild-type embryos, which are enriched in glutamatergic neurons (see above for the method). After 2 weeks of culture, neurons were co-cultured for 16h with PCMs or cell-sorted spinal cord macrophages (see below for the method) in neuron culture medium. The medium was then collected for glutamate quantification, a surrogate of glutamatergic neuron activation. Cells were then washed with PBS and fixed in 4% paraformaldehyde. F-actin was stained overnight at 4°C with Texas Red-X Phalloidin (ThermoScinetific) to visualize cell structure and anti-CD11b APC conjugated (Biolegend) to determine macrophage shape. Digitized images were analyzed with ImageJ and data were expressed as a ratio of fusiform/rounded cells.

Histology. Mice were sacrificed and tissues (epididymal, subcutaneous, brown adipose tissues and liver) were excised and fixed in 4% paraformaldehyde. The tissues were later embedded in paraffin. 6 µm sections were performed using a HM340E microtome (Microm Microtech, Francheville France) and stained with H&E as previously described (Gautier et al., 2013).
- For immunofluorescence, spinal cords were fixed in 4% paraformaldehyde 30% sucrose for 48h and embedded in OCT before sectioning by cryostat. Samples were blocked 30min at room temperature with PBS containing 1% BSA and FC block before incubation with PBS containing 0.2% BSA. Then samples were incubated with either anti-VGLUT3 (Biolegend,

clone 2B9) overnight at 4°C. Next, samples were incubated with secondary antibody (Jackson Immuno Research, anti-mouse IgG Cy5 conjugated) in PBS at RT for 2 hours.
- For immunohistochemistry in paraffin embedded sections: paraffin sections of brown adipose tissue were de-paraffinized and rehydrated by washes in 100% xylene, 100% ethanol, 95% ethanol, 70% ethanol, 50% ethanol, water and then washed in phosphate-buffered saline (PBS). Heat-induced antigen retrieval of sections was carried out IHC Antigen retrieval solution (eBiosciences) and then washed in PBS. Sections were then blocked for 1 hour in blocking buffer (1% BSA, 1% Tween, in PBS), then incubated with anti-Tyrosine hydroxylase alexa fluor 488 conjugated antibody (Abcam) diluted in antibody dilution buffer (1% BSA, 1% Tween, in PBS) overnight at 4°C. Slides were then washed thoroughly and coverslips were mounted with aqueous glue. Sections were observed the following day by fluorescent microscopy.

Adipose tissue cellularity. Cellularity of WAT was determined as previously described (Gautier et al., 2013). Briefly, images of sectionned adipocytes were acquired from a light microscope fitted with a camera, and the measurement of ~400 cell diameters was performed allowing calculation of a mean fat cell weight using the MotionTracking Software (Generous gift from the Zerial Lab MPI-CGB, Dresden, Germany).

Muscle type II fibre type. For tibialis anterior muscle fibre type analysis, sections were immunostained with anti-type II myosin heavy chain (MyHC) monoclonal antibodies (SC-71, 2F7, MHCIIb (BF-F3), Developmental studies hybridoma bank) at 1:500 dilution. The percentage of type II (fast) MyHC fibres were counted per section using Imaris software.

Flow cytometry analysis. Tissues were collected, weighted, shredded with scissors and then incubated for 30 minutes with HBSS medium containing 1.5 mg/ml collagenase A (for adipose tissues) or collagenase D (Roche Diagnostics) at 30°C. The resulting suspension was lysed (BD PharmLyse), centrifuged (400g, 5min at 4°C) and stained for 25 min protected from light. For flow cytometry analysis the following list of antibodies was used: CD45 APC-Cy7 conjugated (clone 30-F11, BD Biosciences), CD64 Brilliant Violet 421 conjugated (clone X54-5/7.1, BioLegend), F4/80 PeCy7 conjugated (clone BM8, BioLegend), CD206 PerCp-Cy5.5 conjugated (clone C068C2, BioLegend), CD301 FITC conjugated (clone ER-MP23, Bio-Rad), Mertk PE conjugated (clone 2B10C42, BioLegend). Cells were then washed, centrifuged and data were acquired on BDFACSCanto flow cytometer. Analysis was performed using FlowJo software (Tree Star).

RNA seq of cell sorted macrophages. After peritoneal lavage with PBS, cells were stained with CD64 Brilliant Violet 421 conjugated (clone X54-5/7.1), ICAM-2 APC conjugated (clone 3C4(MIC2/4)) and CD115 PE conjugated (clone AFS98). These antibodies allowed us to cell-sort the major subset of ICAM2^{+} PCMs (Gautier et al., 2012; Kim et al., 2016). Brain and spinal cord macrophages were purified following tissue digestion with 1.5mg/mL collagenase D in HBSS for 30min at 37°C. Then cells were washed and resuspended in 35% Percoll (Sigma). This solution was gently applied over 70% Percoll and centrifuged for 20min at 2000rpm (room temperature). The middle ring was collected and stained with CD11b Brillant violet 510 conjugated (clone M1/70, BioLegend), CD64 Brilliant Violet 421 conjugated (clone X54-5/7.1, BioLegend), CD45 APC-Cy7 conjugated (clone 30-F11, BD Biosciences), MerTK PE conjugated (clone 2B10C42, BioLegend). Cells were cell sorted on BD FacsAria flow cytometer. Total RNA was extracted with RNeasy Mini Kit (Qiagen) according to the manufacturer's protocol and quality was assessed by Nanodrop (Ozyme). Library construction were conducted as described previously (Jha et al., 2015). Libraries were sequenced at the Centre for Applied Genomics (SickKids, Toronto) using a HiSeq 2500 (Illumina).

Integrated network analyses. PCA analysis, k-means clustering, and volcano plot were performed with Phantasus software (Jha et al., 2015). Significant up and down regulated genes were based on p values and fold change calculated with Phantasus. Network-based integration of metabolite and gene expression datasets was conducted using Shiny Gam as previously described (Jha et al., 2015).

RNA analysis. Total RNA was isolated using the RNeasy Plus Mini kit (QIAGEN) and quantified using a Nanodrop (Ozyme). cDNA was prepared using 10 ng/µl total RNA by a RT-PCR using a high capacity cDNA reverse transcription kit (Applied Biosystems), according to the manufacturer's instructions. Real-time qPCR was performed on cDNA using SYBR Green on StepOne device from Applied Biosystem (France). GAPDH gene expression was used to account for variability in the initial quantities of mRNA. Details on the primers used can be found in Table below.

	Sequences of PCR primers	
	Left (5' to 3')	**Right (5' to 3')**
Adrb3	CAG CCA GCC CTG TTG AAG	CCT TCA TAG CCA TCA AAC CTG
Agrp	AAG CTT TGG CGG AGG TGC TAG AT	AAG CAG GAC TCG TGC AGC CTT ACA
CCL2	CAT CCA CGT GTT GGC TCA	GAT CAT CTT GCT GGT GAA TGA GT
CD68	GAC CTA CAT CAG AGC CCG AGT	CGC CAT GAA TGT CCA CTG
Cidea	TTC AAG GCC GTG TTA AGG A	CCT TTG GTG CTA GGC TTG G
Clec10a	AAA ACC CAA GAG CCT GGT AAA	AGG TGG GTC CAA GAG AGG AT
Dio2	CTG CGC TGT GTC TGG AAC	GGA GCA TCT TCA CCC AGT TT
hmox1	AGG GTC AGG TGT CCA GAG AA	CTT CCA GGG CCG TGT AGA TA
IL1 beta	CAA CCA ACA AGT GAT ATT CTC CAT G	GAT CCA CAC TCT CCA GCT GCA
IL6	GCT ACC AAA CTG GAT ATA ATC AGG A	CCA GGT AGC TAT GGT ACT CCA GAA
Integrin alpha 4 (CD49d)	ACT CCC CAC AGG CCT TTA TT	TCA GTC ACT TCG CAG TTT ATT TG
Maoa	CGG ATA TTC TCA GTC ACC AAT G	ATT TGG CCA GAG CCA CCT A
Mecp2	GAC CAG CTC CAA CAG GAT TC	CCC TGG AGA TCC TGG TCT T
Mrc1	CCA CAG CAT TGA GGA GTT TG	ACA GCT CAT CAT TTG GCT CA
NPY	CCG CTC TGC GAC ACT ACA T	TGT CTC AGG GCT GGA TCT CT
Plxna4	CAG CAA TGT TGT GGT GAT GTT	TAG GAT GGA GAG CGC CTG T
pomc	AGT GCC AGG ACC TCA CCA	CAG CGA GAG GTC GAG TTT G
Ppargc1alpha	TGA AAG GGC CAA ACA GAG AG	GTA AAT CAC ACG CGC TCT T
Prdm16	ACA GGC AGG CTA AGA ACC AG	CGT GGA GAG GAG TGT CTT CAG
Pth2R	CTC TGG CTG ATG CGA GGT	CTG CTA AGA TCG GTG CTT GA
Retnl alpha	CCC TCC ACT GTA ACG AAG ACT C	CAC ACC CAG TAG CAG TCA TCC
Sema6a	CCA GAC GAA CGA GTC CCT AA	TTC TAA AGA GGA TGA TCC AGC AC
Slc6a2	GCG GTT CCC TTA TCT CTG CT	CAG CGT GTA TGG AAT CAG GA
Tyrosine hydroxylase	CCC AAG GGC TTC AGA AGA G	GGG CAT CCT CGA TGA GAC T
TNF alpha	CAC AAG ATG CTG GGA CAG TGA	TCC TTG ATG GTG CAT GA
Ucp1	GGC CTC TAC GAC TCA GTC CA	TAA GCC GGC TGA GAT TCT TGT
Vcam1	TCT TAC CTG TGC GCT GTG AC	ACT GGA TCT TCA GGG AAT GAG T

Quantification and statistical analysis

Statistical analysis.
Data are expressed as mean+/- SEM. Statistical analysis was performed using a 2-tailed t test or ANOVA (with Tukey's post-test analysis) with GraphPad Prism software. A P value ≤ 0.05 was considered as statistically significant.

Data and Code availability. The datasets supporting the current study have not been deposited in a public repository because of a pending patent at the time of submission but are available from the corresponding author on request.

Key resources table

REAGENT or RESOURCE	SOURCE	IDENTIFIER
Antibodies		
Akt (C67E7)	Cell Signaling Technology	4691 RRID:AB_915783
CD115 PE (clone AFS98)	eBioscience	12-1152-82 RRID:AB_465808
CD11b APC (Clone M1/70)	Biolegend	101212 RRID:AB_312795
CD11b Brilliant Violet 510 (cloneM1/70)	Biolegend	101263
CD206 PerCp-Cy5.5 (clone C068C2)	Biolegend	141715
CD301 FITC (clone ER-MP23)	Bio-Rad	MCA2392
CD45 APC-Cy7 (clone 30-F11)	BD Biosciences	557659 RRID:AB_396774
CD64 Brillant Violet 421 (clone X54-5/7.1)	Biolegend	139309 RRID:AB_2562694
c-FOS	Abcam	ab190289 RRID:AB_2737414
F4/80 PE-Cy7 (clone BM8)	Biolegend	123114 RRID:AB_893478
ICAM-2 alexa fluor 647 (clone 3C4(MIC2/4))	Biolegend	105612 RRID:AB_2658040
IgG-Cy5	Jackson Immuno research	715-175-150 RRID:AB_2340819
MerTK PE (clone 2B10C42)	Biolegend	151506 RRID:AB_2617037
Myosin Heavy Chain Type IIA (SC71)	Developmental studies hybridoma bank	SC-71 RRID:AB_2147165
Myosin Heavy Chain Type IIB (BF-F3)	Developmental studies hybridoma bank	BF-F3 RRID:AB_2266724
Phospho-Akt (Ser473)	Cell Signaling Technology	4060 RRID:AB_2315049
Texas Red™-X Phalloidin	Thermofisher	T7471 RRID:AB_2828017.
Tyrosine Hydroxylase	Millipore	AB152 RRID:AB_390204
VGLUT3 (clone 2B9)	Sigma	Discontinued
Chemicals, Peptides, and Recombinant Proteins		
2-Deoxy-D-glucose	Sigma	D6134
6-OHDA	Sigma	162957
B-27 Supplement	Invitrogen	17504-044
bFGF Protein	R&D Biosystems	3139-FB-025
Bovine serum Albumin (BSA)	Sigma	A7030
Bovine serum Albumin (BSA) for neuron culture	Sigma	A8806
Clorgyline	Abcam	ab145646
Collagenase A	Sigma	11088793001
Collagenase D	Sigma	11088882001
D-Glucose	Sigma	G7021

DAPI	Sigma	D9542
Fetal bovine serum	Fisher Scientific	12350273
GlutaMAX-1	Invitrogen,	35050-038
HBSS	Fisher Scientific	14175053
L-Glutamic acid	Sigma	G1251
L-Glutamine	Thermofischer	25030024
Neurobasal-A Medium	Invitrogen	10888-022
PBS 1X	Fisher Scientific	14190169
Penicillin-Streptomycin	Fisher Scientific	15140130
Percoll	Sigma	P1644
PFA 4%	VWR International	9713.1000
Poly-D-Lysine Hydrobromide	Dutscher	354210
Protease from Streptomyces griseus (type XIV)	Sigma	P5147
RPMI medium	Fisher Scientific	31870074
Critical Commercial Assays		
ALT reagent	Biosentec	ALT0102
AST reagent	Biosentec	AST0102
BUN reagent	Biosentec	N.A.
Glutamine/Glutamate-Glo™ Assay	Promega	J8022
High-Capacity cDNA reverse transcription kit	Applied Biosystems	4368814
Insulin Mouse Serum Assay kit	Cisbio	62IN3-PEF
NEFA assay	Fujifilm WAKO	W1W436-91995
Norepinephrine ELISA Kit	Abnova	157KA1891
RNeasy Plus Mini Kit (250)	QIAGEN	74136
Triglycerides assay	Diasys	1 5710 99 10021
Uric Acid Reagent	Biosentec	UA-0102
Deposited Data		
RNAseq	NCBI GEO	GEO: GSE to complete
Experimental Models: Organisms/Strains		
Mouse: CX_3CR1^{GFP}	Jackson Laboratory	005582 RRID:IMSR_JAX:005582
Mouse: Gls1fl/fl	Pr. Stephen Rayport's lab	N.A.
Mouse: $LyzM^{cre}$	Jackson Laboratory	004781 RRID:IMSR_JAX:004781
Oligonucleotides		
See **Table in Method details**		
Software and Algorithms		
FlowJo	Tree Star	N.A.
ImageJ	NIH	N.A.
Phantasus	http://genome.ifmo.ru/phantasus/	N.A.
Prism8	GraphPad	N.A.
StepOne Software v.2.2.2	Applied Biosystem	N.A.
Other		
High Fat Diet	Ssniff	TD88137

References

Artyomov, M.N., A. Sergushichev, and J.D. Schilling. 2016. Integrating immunometabolism and macrophage diversity. *Semin Immunol* 28:417-424.

Boutens, L., G.J. Hooiveld, S. Dhingra, R.A. Cramer, M.G. Netea, and R. Stienstra. 2018. Unique metabolic activation of adipose tissue macrophages in obesity promotes inflammatory responses. *Diabetologia* 61:942-953.

Camell, C.D., J. Sander, O. Spadaro, A. Lee, K.Y. Nguyen, A. Wing, E.L. Goldberg, Y.H. Youm, C.W. Brown, J. Elsworth, M.S. Rodeheffer, J.L. Schultze, and V.D. Dixit. 2017. Inflammasome-driven catecholamine catabolism in macrophages blunts lipolysis during ageing. *Nature* 550:119-123.

Cannon, B., and J. Nedergaard. 2004. Brown adipose tissue: function and physiological significance. *Physiol Rev* 84:277-359.

Cao, Q., J. Jing, X. Cui, H. Shi, and B. Xue. 2019. Sympathetic nerve innervation is required for beigeing in white fat. *Physiol Rep* 7:e14031.

Chechi, K., A.C. Carpentier, and D. Richard. 2013. Understanding the brown adipocyte as a contributor to energy homeostasis. *Trends Endocrinol Metab* 24:408-420.

Choi, M.S., Y.J. Kim, E.Y. Kwon, J.Y. Ryoo, S.R. Kim, and U.J. Jung. 2015. High-fat diet decreases energy expenditure and expression of genes controlling lipid metabolism, mitochondrial function and skeletal system development in the adipose tissue, along with increased expression of extracellular matrix remodelling- and inflammation-related genes. *Br J Nutr* 113:867-877.

Crotti, A., and R.M. Ransohoff. 2016. Microglial Physiology and Pathophysiology: Insights from Genome-wide Transcriptional Profiling. *Immunity* 44:505-515.

Davies, L.C., C.M. Rice, E.M. Palmieri, P.R. Taylor, D.B. Kuhns, and D.W. McVicar. 2017. Peritoneal tissue-resident macrophages are metabolically poised to engage microbes using tissue-niche fuels. *Nat Commun* 8:2074.

Ducuing, H., T. Gardette, A. Pignata, S. Tauszig-Delamasure, and V. Castellani. 2019. Commissural axon navigation in the spinal cord: A repertoire of repulsive forces is in command. *Semin Cell Dev Biol* 85:3-12.

Fischer, K., H.H. Ruiz, K. Jhun, B. Finan, D.J. Oberlin, V. van der Heide, A.V. Kalinovich, N. Petrovic, Y. Wolf, C. Clemmensen, A.C. Shin, S. Divanovic, F. Brombacher, E. Glasmacher, S. Keipert, M. Jastroch, J. Nagler, K.W. Schramm, D. Medrikova, G. Collden, S.C. Woods, S. Herzig, D. Homann, S. Jung, J. Nedergaard, B. Cannon, M.H. Tschop, T.D. Muller, and C. Buettner. 2017. Alternatively activated macrophages do not synthesize catecholamines or contribute to adipose tissue adaptive thermogenesis. *Nat Med* 23:623-630.

Fitzgibbons, T.P., S. Kogan, M. Aouadi, G.M. Hendricks, J. Straubhaar, and M.P. Czech. 2011. Similarity of mouse perivascular and brown adipose tissues and their resistance to diet-induced inflammation. *Am J Physiol Heart Circ Physiol* 301:H1425-1437.

Gautier, E.L., T. Shay, J. Miller, M. Greter, C. Jakubzick, S. Ivanov, J. Helft, A. Chow, K.G. Elpek, S. Gordonov, A.R. Mazloom, A. Ma'ayan, W.J. Chua, T.H. Hansen, S.J. Turley, M. Merad, G.J. Randolph, and C. Immunological Genome. 2012. Gene-expression profiles and transcriptional regulatory pathways that underlie the identity and diversity of mouse tissue macrophages. *Nat Immunol* 13:1118-1128.

Glass, C.K., and J.M. Olefsky. 2012. Inflammation and lipid signaling in the etiology of insulin resistance. *Cell Metab* 15:635-645.

Goldmann, T., P. Wieghofer, M.J. Jordao, F. Prutek, N. Hagemeyer, K. Frenzel, L. Amann, O. Staszewski, K. Kierdorf, M. Krueger, G. Locatelli, H. Hochgerner, R. Zeiser, S. Epelman, F. Geissmann, J. Priller, F.M. Rossi, I. Bechmann, M. Kerschensteiner, S. Linnarsson, S. Jung, and M. Prinz. 2016. Origin, fate and dynamics of macrophages at central nervous system interfaces. *Nat Immunol* 17:797-805.

Gosselin, D., V.M. Link, C.E. Romanoski, G.J. Fonseca, D.Z. Eichenfield, N.J. Spann, J.D. Stender, H.B. Chun, H. Garner, F. Geissmann, and C.K. Glass. 2014. Environment drives selection and function of enhancers controlling tissue-specific macrophage identities. *Cell* 159:1327-1340.

Huang, S.C., B. Everts, Y. Ivanova, D. O'Sullivan, M. Nascimento, A.M. Smith, W. Beatty, L. Love-Gregory, W.Y. Lam, C.M. O'Neill, C. Yan, H. Du, N.A. Abumrad, J.F. Urban, Jr., M.N. Artyomov, E.L. Pearce, and E.J. Pearce. 2014. Cell-intrinsic lysosomal lipolysis is essential for alternative activation of macrophages. *Nat Immunol* 15:846-855.
Ivanov, S., J. Merlin, M.K.S. Lee, A.J. Murphy, and R.R. Guinamard. 2018. Biology and function of adipose tissue macrophages, dendritic cells and B cells. *Atherosclerosis* 271:102-110.
Jaitin, D.A., L. Adlung, C.A. Thaiss, A. Weiner, B. Li, H. Descamps, P. Lundgren, C. Bleriot, Z. Liu, A. Deczkowska, H. Keren-Shaul, E. David, N. Zmora, S.M. Eldar, N. Lubezky, O. Shibolet, D.A. Hill, M.A. Lazar, M. Colonna, F. Ginhoux, H. Shapiro, E. Elinav, and I. Amit. 2019. Lipid-Associated Macrophages Control Metabolic Homeostasis in a Trem2-Dependent Manner. *Cell*
Jha, A.K., S.C. Huang, A. Sergushichev, V. Lampropoulou, Y. Ivanova, E. Loginicheva, K. Chmielewski, K.M. Stewart, J. Ashall, B. Everts, E.J. Pearce, E.M. Driggers, and M.N. Artyomov. 2015. Network integration of parallel metabolic and transcriptional data reveals metabolic modules that regulate macrophage polarization. *Immunity* 42:419-430.
Kajimura, S., B.M. Spiegelman, and P. Seale. 2015. Brown and Beige Fat: Physiological Roles beyond Heat Generation. *Cell Metab* 22:546-559.
Kim, K.W., J.W. Williams, Y.T. Wang, S. Ivanov, S. Gilfillan, M. Colonna, H.W. Virgin, E.L. Gautier, and G.J. Randolph. 2016. MHC II+ resident peritoneal and pleural macrophages rely on IRF4 for development from circulating monocytes. *J Exp Med* 213:1951-1959.
Kratz, M., B.R. Coats, K.B. Hisert, D. Hagman, V. Mutskov, E. Peris, K.Q. Schoenfelt, J.N. Kuzma, I. Larson, P.S. Billing, R.W. Landerholm, M. Crouthamel, D. Gozal, S. Hwang, P.K. Singh, and L. Becker. 2014. Metabolic dysfunction drives a mechanistically distinct proinflammatory phenotype in adipose tissue macrophages. *Cell Metab* 20:614-625.
Lavin, Y., D. Winter, R. Blecher-Gonen, E. David, H. Keren-Shaul, M. Merad, S. Jung, and I. Amit. 2014. Tissue-resident macrophage enhancer landscapes are shaped by the local microenvironment. *Cell* 159:1312-1326.
Liu, P.S., H. Wang, X. Li, T. Chao, T. Teav, S. Christen, G. Di Conza, W.C. Cheng, C.H. Chou, M. Vavakova, C. Muret, K. Debackere, M. Mazzone, H.D. Huang, S.M. Fendt, J. Ivanisevic, and P.C. Ho. 2017. alpha-ketoglutarate orchestrates macrophage activation through metabolic and epigenetic reprogramming. *Nat Immunol* 18:985-994.
Lumeng, C.N., J.L. Bodzin, and A.R. Saltiel. 2007. Obesity induces a phenotypic switch in adipose tissue macrophage polarization. *J Clin Invest* 117:175-184.
Lumeng, C.N., J.B. DelProposto, D.J. Westcott, and A.R. Saltiel. 2008. Phenotypic switching of adipose tissue macrophages with obesity is generated by spatiotemporal differences in macrophage subtypes. *Diabetes* 57:3239-3246.
McNelis, J.C., and J.M. Olefsky. 2014. Macrophages, immunity, and metabolic disease. *Immunity* 41:36-48.
Mills, E.L., B. Kelly, and L.A.J. O'Neill. 2017. Mitochondria are the powerhouses of immunity. *Nat Immunol* 18:488-498.
Morrison, S.F., and C.J. Madden. 2014. Central nervous system regulation of brown adipose tissue. *Compr Physiol* 4:1677-1713.
Muller, P.A., B. Koscso, G.M. Rajani, K. Stevanovic, M.L. Berres, D. Hashimoto, A. Mortha, M. Leboeuf, X.M. Li, D. Mucida, E.R. Stanley, S. Dahan, K.G. Margolis, M.D. Gershon, M. Merad, and M. Bogunovic. 2014. Crosstalk between muscularis macrophages and enteric neurons regulates gastrointestinal motility. *Cell* 158:300-313.
Murray, P.J., J.E. Allen, S.K. Biswas, E.A. Fisher, D.W. Gilroy, S. Goerdt, S. Gordon, J.A. Hamilton, L.B. Ivashkiv, T. Lawrence, M. Locati, A. Mantovani, F.O. Martinez, J.L. Mege, D.M. Mosser, G. Natoli, J.P. Saeij, J.L. Schultze, K.A. Shirey, A. Sica, J. Suttles, I. Udalova, J.A. van Ginderachter, S.N. Vogel, and T.A. Wynn. 2014. Macrophage activation and polarization: nomenclature and experimental guidelines. *Immunity* 41:14-20.
Nguyen, K.D., Y. Qiu, X. Cui, Y.P. Goh, J. Mwangi, T. David, L. Mukundan, F. Brombacher, R.M. Locksley, and A. Chawla. 2011. Alternatively activated macrophages produce catecholamines to sustain adaptive thermogenesis. *Nature* 480:104-108.

Nguyen, N.L., C.L. Barr, V. Ryu, Q. Cao, B. Xue, and T.J. Bartness. 2017. Separate and shared sympathetic outflow to white and brown fat coordinately regulates thermoregulation and beige adipocyte recruitment. *Am J Physiol Regul Integr Comp Physiol* 312:R132-R145.
Nguyen, N.L., J. Randall, B.W. Banfield, and T.J. Bartness. 2014. Central sympathetic innervations to visceral and subcutaneous white adipose tissue. *Am J Physiol Regul Integr Comp Physiol* 306:R375-386.
Nguyen, N.L.T., B. Xue, and T.J. Bartness. 2018. Sensory denervation of inguinal white fat modifies sympathetic outflow to white and brown fat in Siberian hamsters. *Physiol Behav* 190:28-33.
Odegaard, J.I., and A. Chawla. 2015. Type 2 responses at the interface between immunity and fat metabolism. *Curr Opin Immunol* 36:67-72.
Okabe, Y., and R. Medzhitov. 2014. Tissue-specific signals control reversible program of localization and functional polarization of macrophages. *Cell* 157:832-844.
Okabe, Y., and R. Medzhitov. 2016. Tissue biology perspective on macrophages. *Nat Immunol* 17:9-17.
Orava, J., P. Nuutila, M.E. Lidell, V. Oikonen, T. Noponen, T. Viljanen, M. Scheinin, M. Taittonen, T. Niemi, S. Enerback, and K.A. Virtanen. 2011. Different metabolic responses of human brown adipose tissue to activation by cold and insulin. *Cell Metab* 14:272-279.
Pirzgalska, R.M., E. Seixas, J.S. Seidman, V.M. Link, N.M. Sanchez, I. Mahu, R. Mendes, V. Gres, N. Kubasova, I. Morris, B.A. Arus, C.M. Larabee, M. Vasques, F. Tortosa, A.L. Sousa, S. Anandan, E. Tranfield, M.K. Hahn, M. Iannacone, N.J. Spann, C.K. Glass, and A.I. Domingos. 2017. Sympathetic neuron-associated macrophages contribute to obesity by importing and metabolizing norepinephrine. *Nat Med* 23:1309-1318.
Puleston, D.J., M. Villa, and E.L. Pearce. 2017. Ancillary Activity: Beyond Core Metabolism in Immune Cells. *Cell Metab* 26:131-141.
Qiu, Y., K.D. Nguyen, J.I. Odegaard, X. Cui, X. Tian, R.M. Locksley, R.D. Palmiter, and A. Chawla. 2014. Eosinophils and type 2 cytokine signaling in macrophages orchestrate development of functional beige fat. *Cell* 157:1292-1308.
Reitman, M.L. 2017. How Does Fat Transition from White to Beige? *Cell Metab* 26:14-16.
Rosen, E.D., and B.M. Spiegelman. 2014. What we talk about when we talk about fat. *Cell* 156:20-44.
Silva, H.M., A. Bafica, G.F. Rodrigues-Luiz, J. Chi, P.D.A. Santos, B.S. Reis, D.P. Hoytema van Konijnenburg, A. Crane, R.D.N. Arifa, P. Martin, D. Mendes, D.S. Mansur, V.J. Torres, K. Cadwell, P. Cohen, D. Mucida, and J.J. Lafaille. 2019. Vasculature-associated fat macrophages readily adapt to inflammatory and metabolic challenges. *J Exp Med* 216:786-806.
Stanford, K.I., R.J. Middelbeek, K.L. Townsend, D. An, E.B. Nygaard, K.M. Hitchcox, K.R. Markan, K. Nakano, M.F. Hirshman, Y.H. Tseng, and L.J. Goodyear. 2013. Brown adipose tissue regulates glucose homeostasis and insulin sensitivity. *J Clin Invest* 123:215-223.
Stienstra, R., R.T. Netea-Maier, N.P. Riksen, L.A.B. Joosten, and M.G. Netea. 2017. Specific and Complex Reprogramming of Cellular Metabolism in Myeloid Cells during Innate Immune Responses. *Cell Metab* 26:142-156.
Tupone, D., C.J. Madden, and S.F. Morrison. 2014. Autonomic regulation of brown adipose tissue thermogenesis in health and disease: potential clinical applications for altering BAT thermogenesis. *Front Neurosci* 8:14.
Weisberg, S.P., D. McCann, M. Desai, M. Rosenbaum, R.L. Leibel, and A.W. Ferrante, Jr. 2003. Obesity is associated with macrophage accumulation in adipose tissue. *J Clin Invest* 112:1796-1808.
Wolf, Y., S. Boura-Halfon, N. Cortese, Z. Haimon, H. Sar Shalom, Y. Kuperman, V. Kalchenko, A. Brandis, E. David, Y. Segal-Hayoun, L. Chappell-Maor, A. Yaron, and S. Jung. 2017. Brown-adipose-tissue macrophages control tissue innervation and homeostatic energy expenditure. *Nat Immunol* 18:665-674.
Wynn, T.A., A. Chawla, and J.W. Pollard. 2013. Macrophage biology in development, homeostasis and disease. *Nature* 496:445-455.

Xu, H., G.T. Barnes, Q. Yang, G. Tan, D. Yang, C.J. Chou, J. Sole, A. Nichols, J.S. Ross, L.A. Tartaglia, and H. Chen. 2003. Chronic inflammation in fat plays a crucial role in the development of obesity-related insulin resistance. *J Clin Invest* 112:1821-1830.
Xu, X., A. Grijalva, A. Skowronski, M. van Eijk, M.J. Serlie, and A.W. Ferrante, Jr. 2013. Obesity activates a program of lysosomal-dependent lipid metabolism in adipose tissue macrophages independently of classic activation. *Cell Metab* 18:816-830.
Zhu, Y., K. Lyapichev, D.H. Lee, D. Motti, N.M. Ferraro, Y. Zhang, S. Yahn, C. Soderblom, J. Zha, J.R. Bethea, K.L. Spiller, V.P. Lemmon, and J.K. Lee. 2017. Macrophage Transcriptional Profile Identifies Lipid Catabolic Pathways That Can Be Therapeutically Targeted after Spinal Cord Injury. *J Neurosci* 37:2362-2376.